PARTICLE IMAGE VELOCIMETRY AROUND A WALL-MOUNTED HEMISPHERE IN SUPERSONIC FLOW

By

MARIO JUAN RIVERO

A thesis submitted to the

School of Graduate Studies

Rutgers, The State University of New Jersey

In partial fulfillment of the requirements

For the degree of

Master of Science

Graduate Program in Mechanical and Aerospace Engineering

Written under the direction of

Edward DeMauro

And approved by

____

____

____

New Brunswick, New Jersey

May, 2020

ABSTRACT OF THE THESIS

Particle Image Velocimetry Around a Wall-Mounted Hemisphere in Supersonic Flow

by Mario Rivero

Thesis Director:
Edward DeMauro

The flow surrounding a wall mounted hemisphere in supersonic flow at Mach 3.4 was investigated experimentally using stereoscopic particle image velocimetry in the Rutgers University Emil Buhler supersonic wind tunnel. The aim of this investigation was to quantify the basic flow structures associated with a three-dimensional shock boundary layer interaction caused by a hemispherical disturbance. The flow velocity upstream and downstream of a 38 mm radius hemisphere was measured at the spanwise centerline. The flow velocity upstream of a 25 mm radius hemisphere was measured at three spanwise locations: centerline, 1.5 mm off center, and 3.0 mm off center. The velocity fields indicate a significant spanwise velocity component in the hemisphere wake in the separated shear layer. From the velocity fields, turbulent kinetic energy and Reynolds stresses were derived. These quantities indicate a significantly turbulent flow in the wake in the separated shear layer and show evidence of three-dimensional flow structures both upstream and downstream of the hemisphere.

Velocity field measurements upstream of the separation shock wave were used to calculate an estimate for the undisturbed turbulent boundary layer on the ceiling of the Rutgers University Emil Buhler supersonic wind tunnel. Ten streamwise locations were sampled across two spanwise planes and the final boundary layer thickness estimate was δ_{99} =16.52 mm $\pm$ 1.26 mm.

Acknowledgements

To begin, I would like to thank my advisor, Dr. Edward DeMauro, for his guidance throughout my graduate career. I would also like to thank Dr. Jerry Shan and Dr. Francisco Javier Diez Garias for their participation in my thesis committee and for their tutelage throughout my career academic both undergraduate and graduate.

I would like to thank John Petrowski for his continuous assistance in maintaining and repairing the wind tunnel laboratory. His expertise made what would otherwise be large hurdles into small bumps in the road. His willingness to help all the students who came knocking on his door is truly inspiring.

I would like to thank Arastou Pournadali Khamseh and Ramez Kiriakos for helping me operate the wind tunnel and PIV system throughout my research. Troubleshooting operational issues is always challenging, but with great help it becomes an everyday task. I would also like to thank Robert Panco for his work installing the smoke seeder and setting up the PIV system.

Lastly, I would like to thank my family and friends for their unending support throughout my academic career. I could not have done it without them.

Table of Contents

List of Tables

List of Figures

Nomenclature

Variables

a Speed of sound

cp Specific heat at constant pressure

cv Specific heat at constant volume

δ99 Boundary layer thickness

δij Boundary layer thickness

e Internal energy

γ Ratio of specific heats

h Enthalpy

Kn Knudsen number

M Mach number

M∞ Freestream Mach number

μ Dynamic viscosity

μ0 Stagnation dynamic viscosity

P Pressure

P0 Stagnation pressure

R Specific gas constant

Reu Unit Reynolds number

Rij Indexed Reynolds Stress

ρ Fluid density

ρ0 Stagnation fluid density

St Strouhal number

T Temperature

T0 Stagnation Temperature

τij Stress tensor

τp Characteristic particle time scale

u Streamwise velocity

ui Indexed velocity

U∞ Freestream velocity

u'i Indexed velocity fluctuation

v Vertical velocity

w Spanwise velocity

Acronyms

PIV - Particle image velocimetry

SPIV - Stereoscopic particle image velocimetry

TR-PIV – Time resolved particle image velocimetry

SBLI – Shock wave boundary layer interaction

EBSWT - Emil Buhler supersonic wind tunnel

TKE - Turbulent kinetic energy

Chapter 1 Introduction

1.1 Background

1.1.1 Motivation

Since time immemorial military applications have been at the fore of scientific research. Across the history of man lies breath of inventions that have fundamentally changed the face of combat. In the early 20th century one of these inventions claimed the sky as a new frontier. This of course was the airplane. In the short century since its invention the airplane has gone from hardly as fast as a car to breaking the sound barrier with ease. As we march forward advancements like these come more quickly and more abundantly. The next phase of innovation for military aircraft is on the horizon and what exactly that will look like is difficult to say, however there are some key features heavily sought after. Reliable, high-speed, precision weapon systems have been a long-standing goal in military engineering, and the bar on these measures is rising more quickly as time passes.

It is of current interest that modern aircrafts are to be fitted with high-energy deposition laser systems. Such designs will likely have implements, if not an entire housing, protruding from the surface of the aircraft, resulting in a complex three-dimensional shock boundary layer interaction, SBLI. The flow physics involved pose significant design concerns regarding the operation of laser subsystems. Specifically, optical aberrations due to the three-dimensional SBLIs around such protrusions directly reduce the beam quality. This issue is not unique to laser systems. Any optical system protruding from the aircraft surface suffers from these optical aberrations. In order to fully characterize the effects of the SBLI system on the subsystem performance, significant quantitative study of the flow is necessary. To that end, we endeavored to study flow around a hemisphere in supersonic flow. Being a straightforward geometry, the hemisphere can be representative of most rounded protrusions on the surface of supersonic aircraft. Understanding the flow field around a hemisphere can give valuable insight to aid in the design of these and other subsystems. Furthermore, the literature on this flow field is quite limited, so this work seeks to fill some current gaps in experimentation.

1.1.2 Governing Equations

In this section, the governing equations and basic assumptions of the flow physics expected in this study are summarized. Comprehensive derivation of the formulae and explanation of the physical mechanisms can be found in a vast breath of the literature including textbooks.

In this experiment, compressible, supersonic, Newtonian fluid flow has been studied. To fully describe the flow, fluid properties are defined by the ideal gas law as well as the conservation equations for mass, momentum, and energy. We begin with the continuity equation. Derivations obtained from *Fluid Mechanics* by Kundu et al [25] and *Modern Compressible Flow with Historical Perspective* by Anderson [24].

The continuity equation is an application of the conservation of mass to a fluid, in this case a compressible fluid. Continuity states that the rate of change of mass per unit volume is equal to the rate of mass influx per unit volume. The differential form of continuity equation in Cartesian coordinates is given by:

$$\frac{\partial \rho}{\partial t} + \frac{\partial \rho u_i}{\partial x_i} = 0$$

The Navier-Stokes equations are an application of Newton's second law to a fluid. Here we define the conservation of momentum for a compressible flow,

$$\rho\left(\frac{\partial u_i}{\partial t} + (u_i \cdot \nabla)u_i\right) = \nabla \cdot \sigma_{ij} + f_i$$

where σ_{ij} is the stress tensor and f_i is the sum of all body forces.

$$\sigma_{ij} = -p\,\delta_{ij} + \tau_{ij}$$

τ_{ij} represents the stress tensor, which is defined as:

$$\tau_{ij} = (-p + k\nabla \boldsymbol{u})\delta_{ij} + \mu\left(\frac{\partial u_i}{\partial x_j} + \frac{\partial u_j}{\partial x_i} - \frac{2}{3}\frac{\partial u_k}{\partial x_k}\right)$$

where δ_{ij} is the Kronecker Delta tensor, and k is the bulk viscosity coefficient.

$$k = (\lambda + \frac{2}{3}\mu)$$

μ is the dynamic viscosity coefficient and λ is referred to as the second viscosity coefficient. Stokes hypothesis states for Newtonian fluids, such as air, k is negligible.

$$\lambda \sim -\frac{2}{3}\mu$$

Applying the Stokes hypothesis to the momentum conservation equation

$$\rho\frac{\partial u_i}{\partial t} + \rho u_j\frac{\partial u_i}{\partial x_j} = -\frac{\partial p}{\partial x_i} + \frac{\partial}{\partial x_j}\left(\mu\left(\frac{\partial u_i}{\partial x_j} + \frac{\partial u_j}{\partial x_i} - \frac{2}{3}\frac{\partial u_k}{\partial x_k}\right)\right)$$

Third is the conservation of energy. Here we state the First Law of Thermodynamics per unit volume.

$$\rho\frac{\partial}{\partial t}\left(e + \frac{1}{2}\|\boldsymbol{u}\|^2\right) + \rho u_j\frac{\partial}{\partial x_j}\left(e + \frac{1}{2}\|\boldsymbol{u}\|^2\right) =$$

$$\rho\dot{q} + \frac{\partial}{\partial x_j}\left(k\frac{\partial T}{\partial x_j}\right) - \frac{\partial}{\partial x_j}\tau_{ij}u_i$$

For air we assume an ideal gas. This allows us to relate thermodynamic properties via an equation of state. The equation of state for an ideal gas is as follows:

$$p = \rho R T$$

where *R* is the gas constant. For air

$$R = 287\ \frac{J}{kg.\ K}.$$

$$R = c_p - c_v$$

c_p and c_v are the specific heat at constant pressure and the specific heat at constant volume respectively. Specific heats for air are: $c_p = 1005\ \frac{J}{kg.\ K}$ and $c_v = 717.5\ \frac{J}{kg.\ K}$. The ratio of specific heats, γ, is defined as

$$\gamma = \frac{c_p}{c_v}$$

$$\gamma_{air} = 1.4$$

Assuming air to be a calorically perfect gas, the internal energy e and enthalpy h depend only on temperature.

$$e = c_v\, T$$

$$h = c_p\, T$$

Viscosity is defined by Sutherland’s Equation

$$\frac{\mu}{\mu_0} = \frac{T_0 + C}{T + C}\left(\frac{T}{T_0}\right)^{\frac{3}{2}}$$

where $\mu_0 = 1.789 \times 10^{-5}\,\frac{kg}{m \cdot s}$ and Sutherland’s Constant C = 110.3 for air at a temperature of $T_0 = 288\ K$.

We assume a quasi-1D flow in the wind tunnel until a disturbance is encountered. Up to this point we further assume the flow is adiabatic and reversible, isentropic. The relationship between the stagnation properties and static properties can be defined under these assumptions.

$$\frac{T_0}{T} = 1 + \frac{\gamma - 1}{2} M^2$$

$$\frac{p_0}{p} = \left(1 + \frac{\gamma - 1}{2} M^2\right)^{\frac{\gamma}{\gamma - 1}}$$

$$\frac{\rho_0}{\rho} = \left(1 + \frac{\gamma - 1}{2} M^2\right)^{\frac{1}{\gamma - 1}}$$

where M is the Mach number and the subscript 0 indicates stagnation properties. The Mach number is defined as the ratio of magnitude of velocity to the speed of sound:

$$M = \frac{\|\boldsymbol{u}\|}{a}$$

$$a = \sqrt{\gamma R T}$$

Shock Waves

When the flow is accelerated beyond Mach 1 an important transition occurs. The flow speed exceeds the speed at which information can propagate upstream. As a result, flow disturbances are not navigated smoothly. Instead, the flow is turned almost immediately upon encountering an obstacle. This creates a thin region where the Mach number, pressure, density, and temperature change very rapidly. This region is called a shock wave.

We can define the relationship among thermodynamic properties across a shockwave. In the case of a shockwave which is normal to the flow direction, a normal shock, we have the following relations

$$\frac{P_2}{P_1} = 1 + \frac{2\gamma}{\gamma + 1}(M_1^2 - 1)$$

$$\frac{T_2}{T_1} = \left(1 + \frac{2\gamma}{\gamma + 1}(M_1^2 - 1)\right)\left(\frac{2 + (\gamma - 1)M_1^2}{(\gamma + 1)M_1^2}\right)$$

$$\frac{\rho_2}{\rho_1} = \frac{(\gamma + 1)M_1^2}{2 + (\gamma - 1)M_1^2}$$

$$M_2^2 = \frac{1 + \frac{\gamma - 1}{2}M_1^2}{\gamma M_1^2 - \frac{\gamma - 1}{2}}$$

The literature over the last 100 years covers the properties of shock waves in great detail. Further discussion of properties related to normal, oblique, and detached shockwaves can also be found in "Modern Compressible Flow with Historical Perspective" [24].

Boundary Layer

Due to the no slip condition at the wall boundary, we observe a region extending some distance away from the boundary where the flow velocity is significantly lower than that of the freestream. Within this region viscous forces in the flow are prominent. This region is referred to as the boundary layer. The boundary layer has been the subject of a plethora of experiments and computational analysis. In this section, a brief overview of the relevant relationships regarding a compressible turbulent boundary layer as seen in the wind tunnel.

Inner Layer

The boundary layer can be divided into two regions a viscous inner layer and an inviscid outer layer. As presented by Ojala et al [12]. The inner layer can be described by the incompressible Law of the Wall using a Van Driest velocity scaling to address the compressibility effects.

$$\frac{u^*}{u_\tau} = \frac{1}{k}\log(\frac{yu_\tau}{\nu_w}) + C^*$$

$$u^+ = \frac{u^*}{u_\tau} \quad y^+ = \frac{yu_\tau}{\nu_w}$$

$$u^\star = \frac{u_e}{b}\sin^{-1}\left(\frac{2b^2\frac{\overline{u}}{u_e} - a}{\sqrt{\left(a^2+4b^2\right)}}\right)$$

$$a = \left(1 + r\frac{\gamma-1}{2}M_e^2\right)\frac{T_e}{T_w} - 1$$

$$b = \sqrt{r\frac{(\gamma-1)}{2}M_e^2\frac{T_e}{T_w}}$$

$$r = .89$$

$$M_e = \sqrt{\gamma R T_e}$$

Where $u^+$is the scaled velocity, and $y^+$is the viscous wall unit.

Outer Layer

In the outer layer we refer to the Law of the Wake

$$\frac{\overline{u}}{u_T} = \frac{1}{\kappa}\log\left(\frac{yu_T}{\nu}\right) + C + \frac{\Pi}{\kappa}w\left(\frac{y}{\delta}\right)$$

$$w\left(\frac{y}{\delta}\right) = 2\sin^2\left(\frac{\pi y}{2\delta}\right)$$

Where Π is Coles parameter which defines the strength of the deviation from a logarithmic profile. Coles parameter is 0.55 for boundary layers with Re_θ > 5000.

1.1.3 Shock Boundary Layer Interactions

Shock wave boundary layer interactions, SBLIs, describe complicated events observed across a broad range of flows in which a shockwave impinges on the boundary layer. In application some examples can include transonic/high-speed airfoils, aircraft control surfaces, overexpanded nozzles and supersonic inlets, such as in a ramjet. Some simpler examples of SBLIs are flows past compression ramps, blunt or sharp fins, wedges, cylinders and hemispheres.

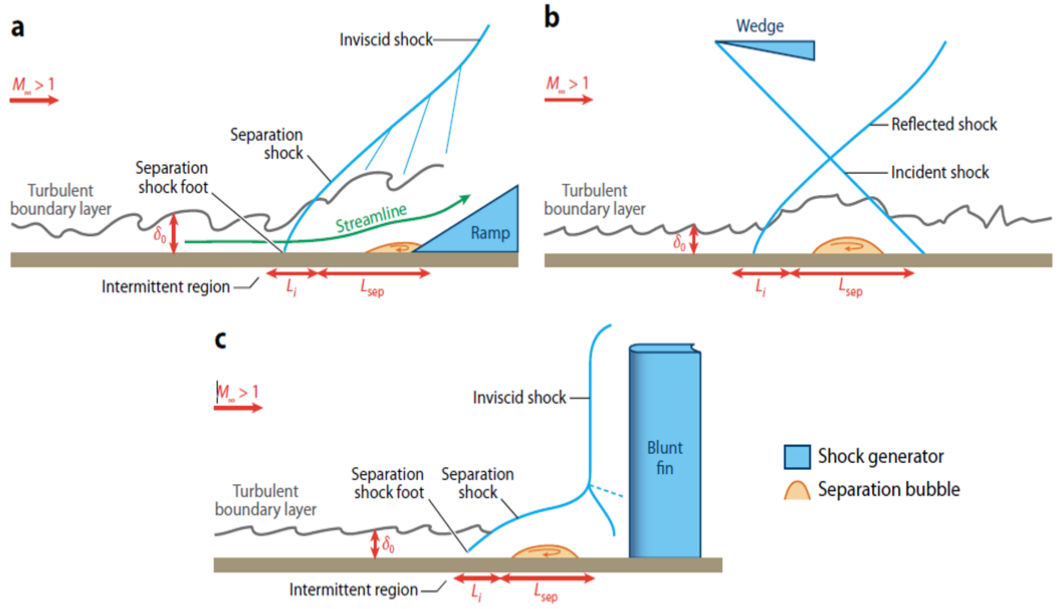

Fig.1 2-D Compression Ramp (a), Wedge (b), Blunt Fin (c) SBLIs Taken from (Clemens 2012)

In all these cases when flow disturbances exceed a certain threshold, when the ramp angle exceeds a certain value in the case of the compression ramp for example, the shock stands off from the body. The point at which the shock terminates within the boundary layer is called the shock foot. At the shock foot, an adverse pressure gradient develops, forcing the flow near the wall upstream causing the boundary layer to separate from the wall. As the flow separates an inviscid instability forms at the shear layer which leads to the formation of vortices which grow as they travel downstream. This is the well-studied Kelvin Helmholtz instability. These vortices impart a net downward momentum to the separated flow and as they travel downstream, they grow large enough to impart sufficient momentum to force the boundary layer back down until it reattaches to the surface. As the vortices travel downstream, they move downward and if they reach below the sonic line, they can propagate upstream. This creates a region of recirculating flow known as the separation bubble.

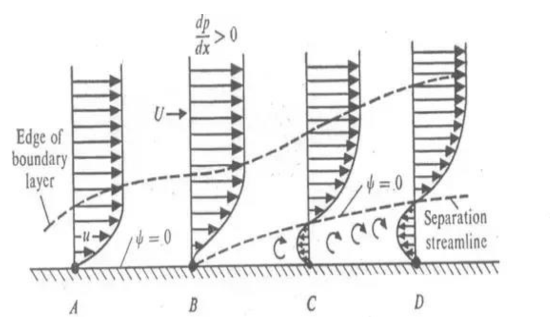

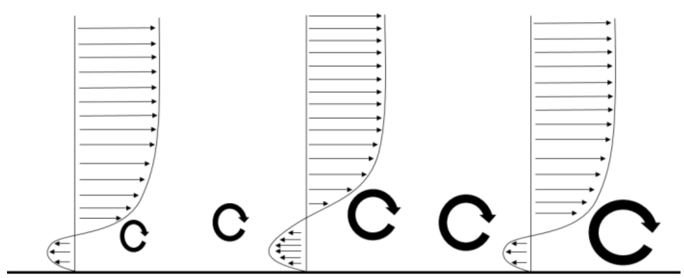

Fig. 2 Boundary Layer Separation **Fig. 3 Separation Vortex Convection and Growth**

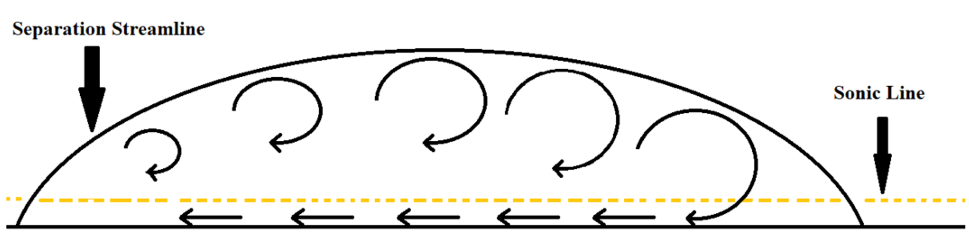

Fig. 4 The Separation Bubble

The shockwave commonly initiates a considerable boundary layer separation leading to significant unsteadiness. Instability in the system drives the shock foot to oscillate in the streamwise direction and causes the separation bubble to grow and shrink. Moreover, the oscillatory motion of the shock foot and separation bubble have been shown to be highly correlated [18].

For the case of a wall mounted hemisphere a three-dimensional SBLI is observed. As shown in figure 5, a separation shock forms some distance upstream of the hemisphere. An adverse pressure gradient forms across the shock, leading to boundary layer separation at the shock foot. While this phenomenon is not unique to three-dimensional bodies and is observed in two-dimensional bodies such as compression ramps and wedges[18-19], the hemisphere shock structures are themselves three-dimensional unlike that of other canonical flows such as 2-D compression ramps. In the region immediately downstream of the separation shock the flow is separated and a separation bubble is formed. Further downstream the boundary layer reattaches and a secondary inviscid shockwave forms redirecting the flow around the hemisphere surface. These shock waves intersect above the hemisphere surface as shown. The separation shock foot moves in oscillatory motion along the surface in a region defined by Clemens et al as the intermittent region, L_i.

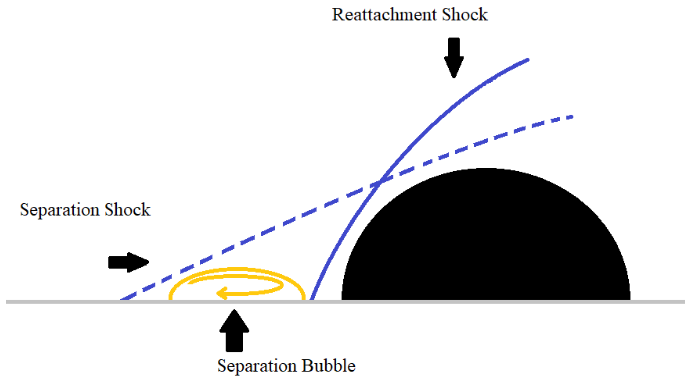

Fig. 5: Fundamental Flow Structures Around a Hemisphere in Supersonic Flow at the Spanwise Center

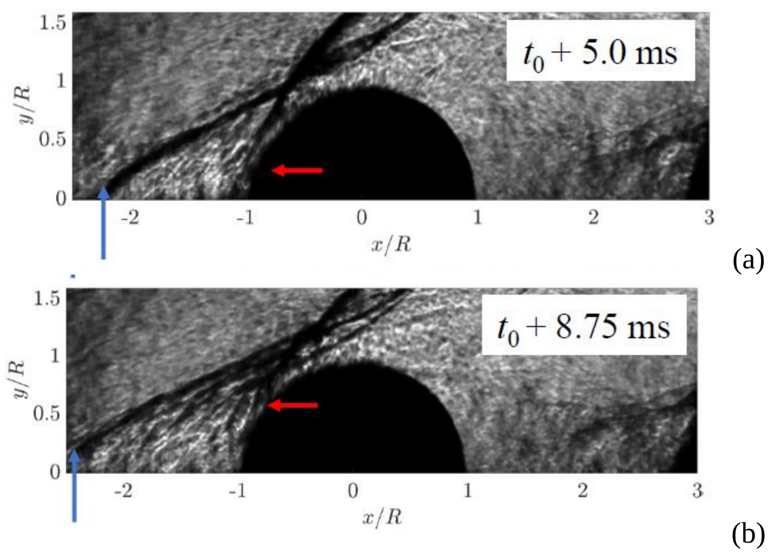

Fig. 6 Schlieren Photography of Flow Around a Hemisphere at a time 5.0 ms (a) and 8.75 ms (b) Note the frames show the motion of both the upstream separation shock and the downstream reattachment shock for the case of a wall mounted hemisphere. Taken from DeMauro (2018)[14]

For high-speed aircraft applications this unsteadiness can cause buffeting, inlet instability, thermal loading, and structural fatigue. Furthermore, when an optical instrument is needed, looking through an unsteady SBLI system can prove challenging as the unsteady motion of the shockwave causes unsteady changes in the direction of light passing through the shockwave. The driving mechanism(s) behind the unsteady motion have yet to be fully understood and pose a significant impedance to the design of high-speed aircraft laser systems and other optical instrumentation. Therefore, further study into the wall-mounted hemispheres and other similar flow fields is certainly warranted.

1.2 Literature Review

SBLIs are dependent on several parameters, such as boundary layer thickness, Reynolds number, Mach number, and disturbance geometry. As presented by Delery and Marvin[1], Dolling[10] showed that the boundary layer to diameter ratio showed little affect across a broad range of values, between 0.26 and 5.3. Furthermore, Sedney & Kitchens[11], in their work, also observed a weak dependence on the boundary layer thickness. They did observe a dependency on the obstacle height of the location of the separation point upstream of the obstacle.

1.2.1 Driving Mechanism for Unsteady motion

Several comprehensive reviews have been published discussing the past work studying SBLIs in a variety of flows. Clemens et al [18] discusses the work of the last several decades looking specifically into the mechanism driving the unsteady motion of the separation bubble and separation shock foot. They find that the literature converges on two possible driving mechanisms, propagation of unsteadiness in the upstream boundary layer, and an intrinsic unsteadiness of the flow in the separation bubble.

As presented by Clemens et al [18], Plotkin (1975) proposed a mathematical model assuming the shock is convected by velocity fluctuations in the upstream boundary layer and it tended to restore to its mean location. This was attributed to the stability of the mean flow. Experimental wall-pressure data by Poggie and Smits (2001) were consistent with Plotkin’s model, except for regions characterized by low-frequency pressure fluctuations. Touber and Sandham (2011) developed a first-order model of the system. They showed large scale motions of the interaction were consistent with those observed experimentally and numerically, when the system was forced with white noise. The upstream boundary layer is a natural source of broadband velocity fluctuations which could serve as the driver for this low-frequency motion.

A correlation between the shock foot velocity and the pressure fluctuations in the upstream boundary layer was observed Erengil and Dolling (1993). They found the upstream unsteadiness preceded the shock foot motion, implying a possible upstream causation. In fact, the same correlation was observed in flow over a swept compression ramp, however, the pressure measurements under the intermittent and separated regions indicated the separation bubble motion preceded the shock foot motion, implying a possible downstream causation. The investigators thus concluded that two mechanisms are likely at play, the convection of high frequency unsteadiness from the upstream boundary layer, and large-scale pulsations of the separation bubble.

Some studies, present a strong argument for the downstream unsteadiness to be the primary driver of the shock foot motion. While Erengil & Dolling (1991a, 1993b), Gramman & Dolling (1990), and Brusniak & Dolling (1994) observed distinct correlations between pressure fluctuations in the upstream boundary layer and shock-foot unsteadiness, they also reported correlations between shock-foot motion and pressure fluctuations under the separation bubble. Moreover, the downstream pressure fluctuations were observed to precede the shock-foot motion. While this may imply the downstream flow is forcing the motion of the shock foot, Brusniak & Dolling (1994) pointed out that these studies do not establish this definitively. The convected upstream unsteadiness could be the causing the downstream fluctuations to begin with, and the downstream fluctuations in turn inducing the shock foot motion.

Piponniau et al. (2009) proposed a model of separation bubble unsteadiness that explicitly assumes the importance of the shear layer in terms of its entrainment characteristics. Under the assumption that the shear layer entrains the low momentum fluid out from the separation bubble, and that the amount of mass in the bubble is constant if time averaged, they suggest there must be a mechanism by which the mass of the separation bubble is replenished. They proposed that such a mechanism could be correlated to large-scale of the shear layer near the mean reattachment points.

Wu &Martin (2008) looked at the flow over a compression ramp at Mach 2.9 using DNS. They suggest the shock foot motion may be driven by a shear layer instability. They argue the shear layer may flap in response to an imbalance in either or both the entrainment rate of the shear layer and the separation bubble recharge rate near reattachment. Priebe & Martin (2012) also studied compression ramp flow at the same Mach number using DNS. Their results corroborated the findings of Wu &Martin (2008) and others on the dominant role of separation bubble pulsations on the separation shock motion. They showed significant changes in the streamline organization, shear layer turbulence levels, and the size of the separation bubble, at different phases of SBLI unsteadiness.

While a consensus has yet to be reached, the literature to date seems to find influence from both upstream and downstream fluctuations to be significant contributors to the unsteady shock foot motion. Still, it appears that the downstream mechanism is dominant for more strongly separated flows, with larger separation bubbles. This can possibly be attributed to increased strength of downstream vortices in larger bubbles as they have more room to grow before propagating upstream.

1.2.2 Hemisphere SBLI

As of now, while some CFD analysis has been done, this flow field has received little experimental inquiry. This study seeks to quantitatively measure the characteristic of the flow field surrounding a hemisphere subject to a freestream Mach number of 3.4.

Although several studies have looked at this basic flow field, they have been primarily focused on the use of hemispheres as discrete roughness elements for initiating turbulent transition within a laminar boundary layer. Such studies use hemispheres of radii close to or less than the boundary layer thickness, $\frac{\delta_{99}}{R} \gtrsim 1$. While certain flow features are common throughout, these studies do not provide enough investigation of the flow field for the case of a typical large protrusion. Furthermore, the unsteady characteristics of the three-dimensional shock boundary layer interaction caused by a hemisphere requires a significant amount of further study.

Computational work by Morgan et al [8-9] considered supersonic flow past a hemisphere at Mach 2.0. They compared computational analyses using RANS, DDES, and LES methods, and showed some small scale vortical structures propagating downstream along the surface of the hemisphere. Unsteady motion of the separation shock foot was observed. No quantification of the boundary layer thickness with respect to the radius of the hemisphere was provided.

Experimental studies of this flow field have largely focused on the transonic regime. Work by Gordeyev et al [4] visualized many of the basic flow features and their evolution from subsonic to transonic speeds, $0.2 < M_\infty < 0.7$. They recorded oil luminance from several cameras at different angles, and using a perspective transformation matrix technique, reconstructed a three-dimensional rendering of the oil flow patterns. This rendering could then be viewed from angles not available in the original recordings. Specifically, they identified the formation of a large vorticial structure appearing along the separation line near the bottom of hemisphere.

Most recently, Beresh et al [20] studied the unsteady wake downstream of a hemisphere with a radius of 25.4 mm subject to Mach numbers of 1.5 and 2.0. Using time resolved particle image velocimetry, TR-PIV, they observed a noticeable oscillatory motion of the shear layer. The hemisphere in these experiments was sitting in and extending through the otherwise undisturbed boundary layer in the wind tunnel. The boundary layer thickness in each case was δ_{99} = 12.4 mm and 10.5 mm respectively for M_∞= 1.5 and 2.0. This places the ratio, $\frac{\delta_{99}}{R}$, of these experiments at 0.49 and 0.41 respectively. They note the way the velocity field in the separated flow aft of the hemisphere presents leads to the possibility of a two-lobe recirculation region. This contrasts previous work by Beresh et al [3] which studied the flow aft of a hemisphere at Mach 0.8 which showed a more conventional recirculating flow.

Wang et al [6] also observed similar oscillatory phenomena in their study of flow past a hemisphere of radius 10 mm subject to a Mach 2.68 freestream. Using nanoparticle-based laser scattering, they studied the propagation of largescale vorticial features as they moved downstream in the wake of the hemisphere. $\frac{\delta_{99}}{R}$, for this experiment is given as 0.4 which is very close to that of the work by Beresh et al.

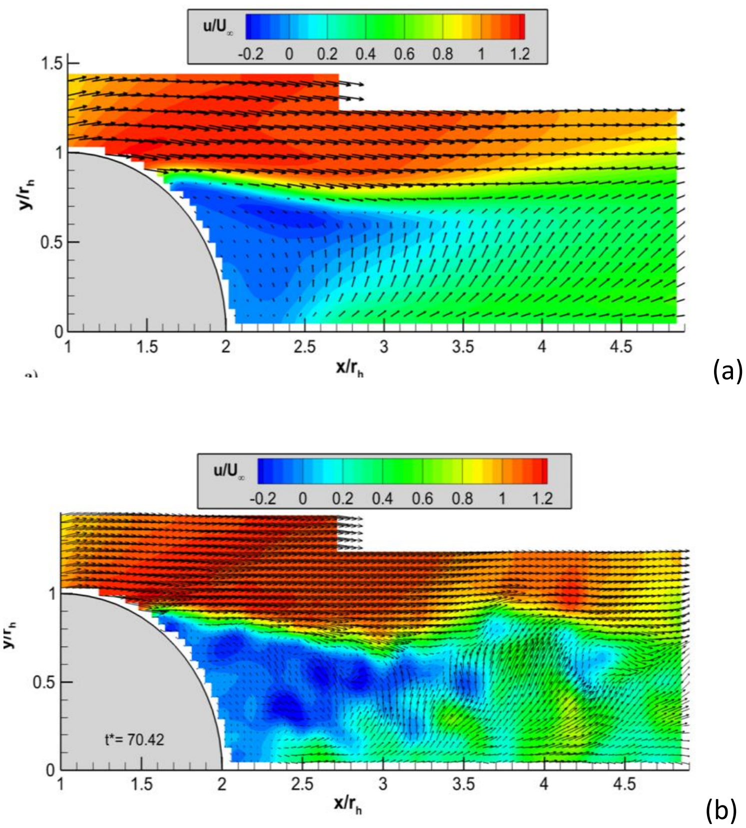

Fig.7 Time Averaged (a) and Intantaneous (b) PIV of Hemisphere Wake Flow at Mach 1.5 Taken from Beresh et al (2019)

Work by DeMauro et al [14] sought to image the unsteadiness in the shock structures surrounding a hemisphere. Specifically, they conducted high-speed schlieren imaging around two hemispheres. This study showed the position of the shock feet of both the separation and reattachment shocks oscillating along the surface with a low frequency in the range of hundreds of Hz. The shock foot of the reattachment shock was shown to move a much greater distance along the surface of the hemisphere than the separation shock. This study was carried out using hemispheres of radii 25.4mm and 31.8 mm, which showed a high degree of similarity in the flow structures presented. The freestream Mach number in the test section was 3.4.

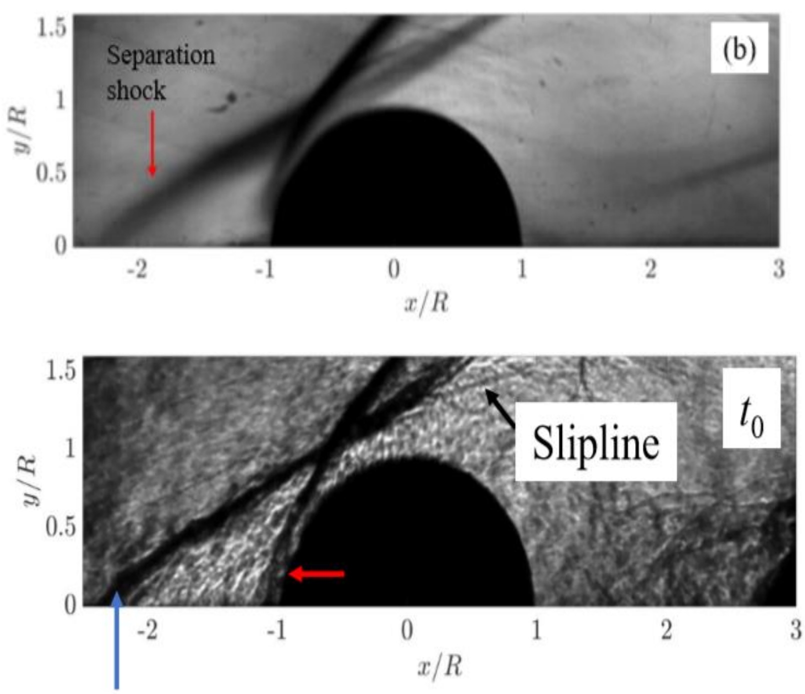

Fig. 8 Time Averaged (top) and Intantaneous (bottom) Schlieren Photography of Hemisphere Flow at Mach 3.4 Taken from DeMauro (2018)

1.2.3 Research Objective

Design of aircraft subsystems with blunt protrusions will be improved by further study of this as well as other three-dimensional flows. Up to this point there is little quantitative data on the subject, as the three-dimensional nature of the flow structures provides a considerable challenge in making quantitative measurements. This work seeks to provide a preliminary quantitative study of the flow field around of a hemisphere using stereoscopic particle image velocimetry, SPIV.

1.3 Particle Image Velocimetry

In this section a brief overview of particle image velocimetry is presented. A more in-depth discussion of the particle image velocimetry method as well as the exact set up used in this experiment can be found in chapter 2.

Particle Image Velocimetry, PIV, is an optical method used to determine the velocity field in a flow by comparing successive images of visible particles present in the flow and calculating the most statistically probable direction and magnitude of their average velocity between the images. The technique was first conducted via opto-mechanical processing, using film photography, however its usefulness was improved immensely by the advent of digital photography. A comprehensive overview of the digital particle image velocimetry method is provided by Willert and Gharib [15].

Digital images are discretized into pixels of finite size which are assigned values corresponding to the color and intensity of the light in view. For the purposes of PIV, only the intensity is of interest. A region of locally high light intensity in an image corresponds to the location of a particle in the flow. By shifting one of the images and conducting a cross-correlation we obtain a value corresponding to how well the particles in the images line up. Iteratively shifting the image by a different number of pixels in either direction allows for a peak cross-correlation value to be found. This peak implies the particles best line up when shifted in that way and thus the vector corresponding to that shift most likely points in the direction of the average velocity of that frame. The magnitude of the average velocity is obtained using the time difference between the pictures and a pixel to true length reference.

In the simplest case, a single camera, oriented perpendicular to the flow, measures the streamwise and vertical components of velocity. A search algorithm conducts a cross-correlation on two successive images, shifts one image by one pixel, and repeats. After searching the entire image domain, a maximum, peak, cross-correlation is identified. It is the shift that resulted in this peak cross-correlation that is determined to be the position vector from the particles' initial location to their final location.

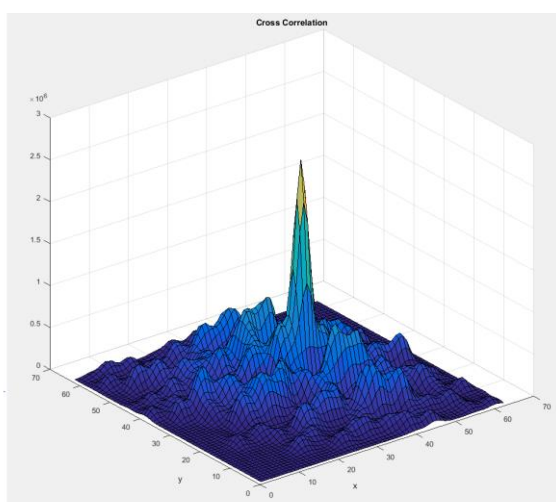

Fig. 9: 2-D Cross Correlation Peak

The peak cross-correlation, however, yields the most statistically likely velocity vector. An important factor to consider is the peak ratio, Q. Q is the ratio of the value of the highest peak to the second highest. A low peak ratio indicates a low certainty between which peak shows the true velocity vector.

As the cameras can only capture a two-dimensional image, only one planar section of the flow can be imaged at a time. To enable imaging of interior sections, a planar light source is required to illuminate only the region of interest. This light source is typically a pulsed laser beam which is expanded into a sheet using a cylindrical lens.

Each image can be split into many smaller, interrogation windows. The cross-correlation peak search algorithm can be applied to each corresponding interrogation window set rather than the entire images. Minimizing the interrogation window size maximizes the spatial resolution of the velocity vector field measured. It should be noted that reducing window size also reduces the number of particles contained in each window, and if this number falls below a certain threshold, the accuracy of the cross-correlation is compromised.

Further, the cross-correlation peak can be interpolated to achieve sub-pixel accuracy. Assuming a Gaussian distribution of the light intensity from the center of the particle, the following equation can be used to adjust the calculated velocity field.

Applying the following equations, the intensity peak location, which corresponds to the center of the particle, can be determined between pixels.[16]

$$f(x) = Ce^{\left(-\frac{(x_0-x)^2}{k}\right)}$$

$$x_0 = i + \frac{\ln(R_{i-1,j}) - \ln(R_{i+1,j})}{2\ln(R_{i,j-1}) - 4\ln(R_{i,j}) + 2\ln(R_{i,j+1})}$$

$$y_0 = j + \frac{\ln(R_{i,j-1}) - \ln(R_{i,j+1})}{2\ln(R_{i-1,j}) - 4\ln(R_{i,j}) + 2\ln(R_{i+1,j})}$$

Where R is the maximum value of the cross correlation located at a point (i, j).

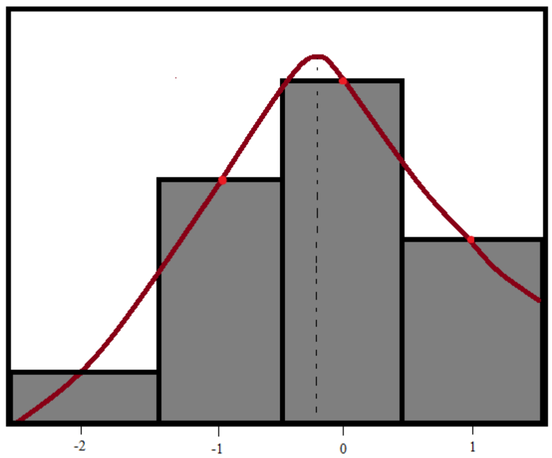

Fig. 10: 3-Point Gaussian Peak Detection

In order to measure the spanwise component of velocity, a stereoscopic particle image velocimetry, SPIV, set up with two cameras is required. The spanwise component cannot be imaged directly but must be derived from two images at some angle relative to the spanwise axis. The two cameras individually capture data of the velocity relative to their orientation, however since the camera orientation is known, the third component of velocity can be decoupled from the other two.

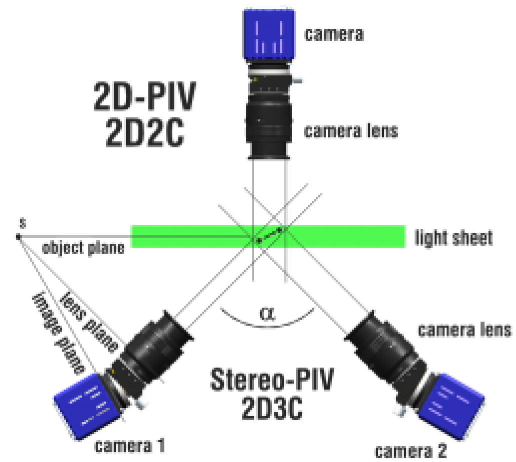

Fig. 11 Planar and Stereo PIV Camera Orientation [27]

1.3 Particle Response

As mentioned, PIV does not measure the flow directly, but instead attempts to track the motion of particles within the flow. In order to ensure accurate measurements of the flow velocity, the seed particles must faithfully follow the flow. To track this capability, we examine the input response time of the particles which can be quantified via the Stokes number, given below. Smaller Stokes numbers indicate shorter response times and thus a more accurate following of the flow. In order to follow the flow in the areas of interest which yield the highest velocity gradients a Stokes number much lower than 1 is required. As presented by, Panco and DeMauro [26]

$$St = \frac{\tau_p}{\tau_f} \ll 1$$

Where τ_p and τ_f are the characteristic time of the particle and fluid, respectively. A modified Stokes drag law can be used to define the particle response time as [17]

$$\tau_p = \frac{\rho_p d_p^2}{18\mu_f}\left(1 + 2.7\mathrm{Kn}_p\right)$$

where the Knudsen number, the ratio of the mean free path to particle diameter, is given by

$$\mathrm{Kn}_d = \frac{kT}{\sqrt{2}\pi d^2 P}\frac{1}{d_p}$$

The time scale of the flow is given by

$$\tau_f = \frac{\delta}{u_\infty}$$

Previous work by Ojala et al [12] measured the boundary layer thickness in the EBSWT. Using the values from their study for δ and u_∞ and the particle diameter advertised by the manufacturer, the Stokes number was predicted to be ~0.09.[12]

Chapter 2 Experimental Facilities

2.1 Overview

SPIV measurements were taken around a 25 mm and a 38.1 mm radius hemisphere mounted to the ceiling of the Emil Buehler supersonic wind tunnel, henceforth referred to as EBSWT. The flow is seeded with atomized mineral oil at a temperature of 390 °F (472 K). A 532 nm Nd: YAG Laser illuminates the seed particles in the flow. The laser is timed in sequence with two LaVision sCmos cameras; all controlled via a Stanford Research Systems DG-535 digital delay generator and LaVision DaVis v8.4 software. This system operates at a repetition rate of 15 Hz, each camera capturing 15 sets of images per second. A set of images consists of two images which are 0.5 μs apart. Image processing and cross-correlation is then conducted using LaVision DaVis v8.4 to obtain velocity vector fields and scalar contours for velocity components, turbulent kinetic energy, and Reynolds stresses.

2.2 Wind Tunnel

The Rutgers University EBSWT has a blow-down design with an exhaust into atmospheric pressure. The tunnel has a one-sided asymmetric nozzle which generates a Mach number of 3.4 in the test section. The test section has a square 6 in. x 6 in. cross sectional area.

Four high pressure (16.6 MPa) air tanks supply compressed air up to 13.8 MPa (2000 psia) to the wind tunnel. The air is pressurized using a four stage Mako compressor which passes air through a Bauer high pressure regenerative dryer, removing any moisture, before supplying it to the tanks.

During operation the stagnation pressure in the tunnel is 120 psi (0.83 MPa). The stagnation temperature is dependent on the ambient temperature outside where the tanks are kept. At a nominal stagnation temperature of 60°F (~289 K), the flow velocity in the test section is ~ 639 m/s. The tunnel exhausts through the roof of the laboratory. The operational parameters of the wind tunnel are summarized in table 1.

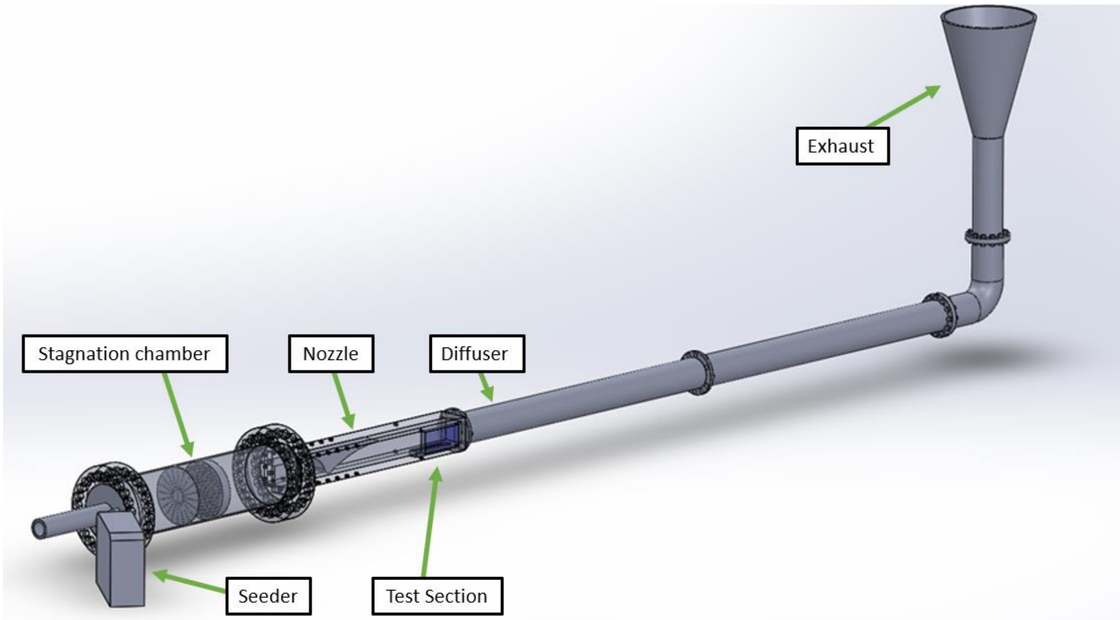

Fig. 12: The Rutgers University Emil Buhler Supersonic Wind Tunnel (not to scale)

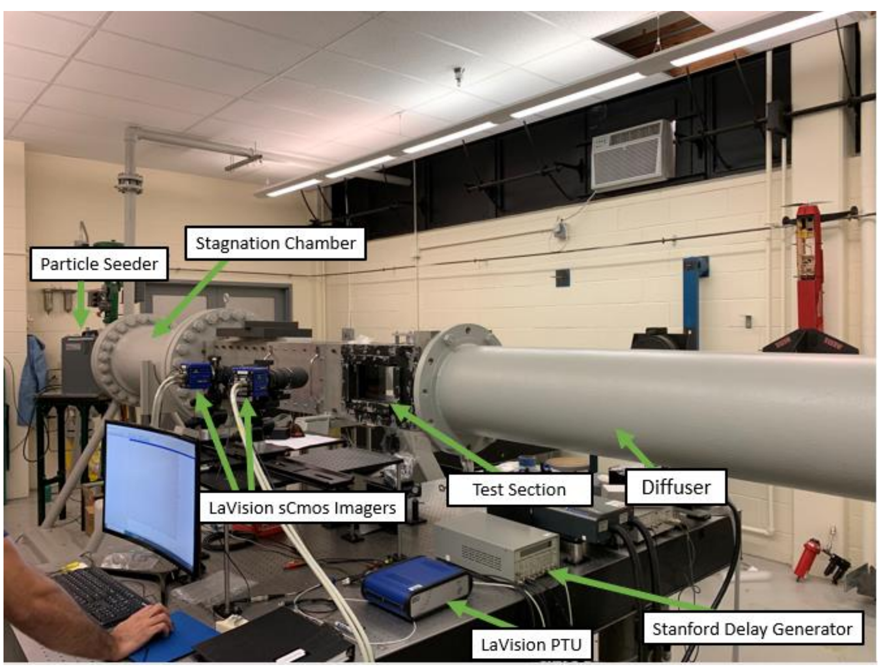

Fig. 13: The Rutgers University Emil Buhler Supersonic Wind Tunnel Laboratory

Table 1: Wind Tunnel Parameters

M_∞	3.4
$T_0{}^*$	~289 K
P_0	0.83 MPa
ρ_0	$1.225\ \frac{kg}{m^3}$
$\mu_0{}^{**}$	$\sim 1.793 \times 10^{-5}\ \frac{kg}{m \cdot s}$
Re_u	$5.82 \times 10^7\ m^{-1}$
U_∞	$640\ {}^{m}/_{s}$
Runtime	<20 s

* Stagnation temperature is dependent on ambient temperature which can realistically vary from 250 K to 310 K throughout the year.

** The viscosity varies with the temperature as given by Sutherland's equation

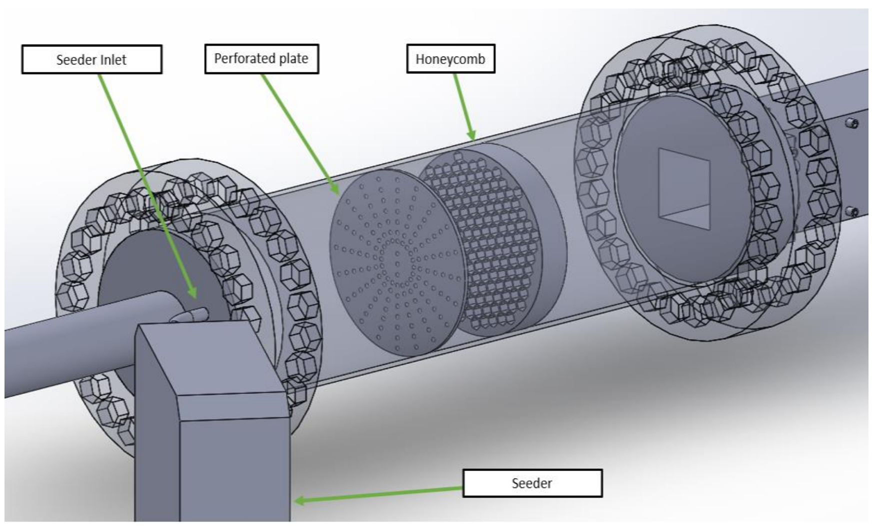

Fig. 14: The Stagnation Chamber

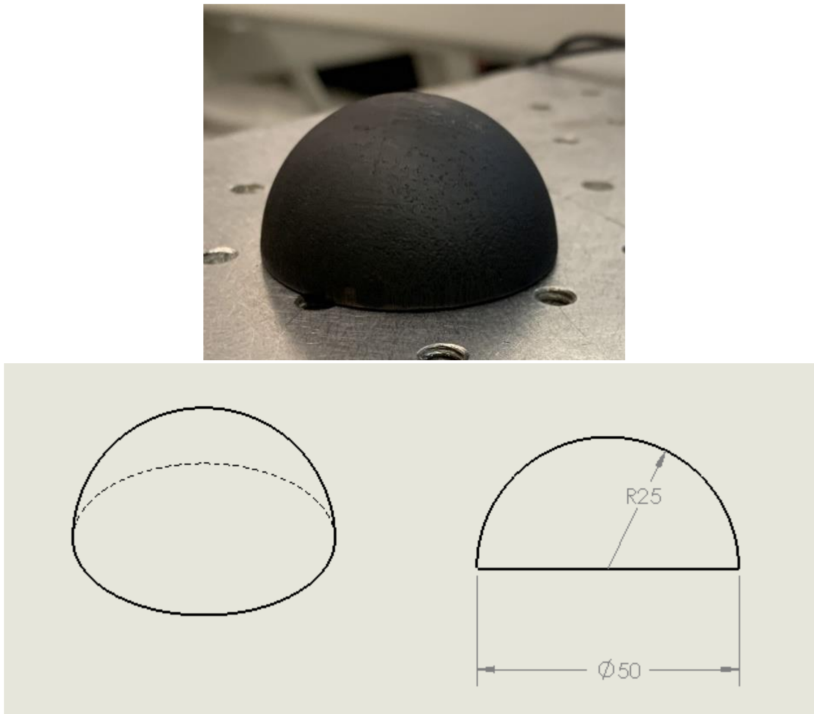

Fig. 15: Hemisphere Test Article

25 mm radius hemisphere model. The model was fixed to the top of the test section and painted black to mitigate any reflections of the laser sheet.

2.3 Seeding

In the EBSWT, a ViCount mineral oil smoke generator supplies atomized mineral oil droplets into the stagnation chamber of the wind tunnel. The smoke generator is plumbed directly into the stagnation chamber, upstream of the blast plate and flow straighteners. When the tunnel is operated mineral oil in the seeder is atomized and flows into the stagnation chamber via pressurized nitrogen. The seeder is capable of outputting 850 $\frac{mg}{s}$ of oil at pressures up to ~1.0 MPa relative to the stagnation pressure.

During operation the nitrogen reservoir driving the flow of mineral oil into the tunnel is set to 15 bar (1.5 MPa). The seeder operates at an internal temperature of 390 °F = 472 K. As previously stated, the average particle diameter as stated by the manufacturer is 0.3 μm which results in a Stokes number of ~0.09 when calculated using δ and u_∞ measured by Ojala et al.[12]

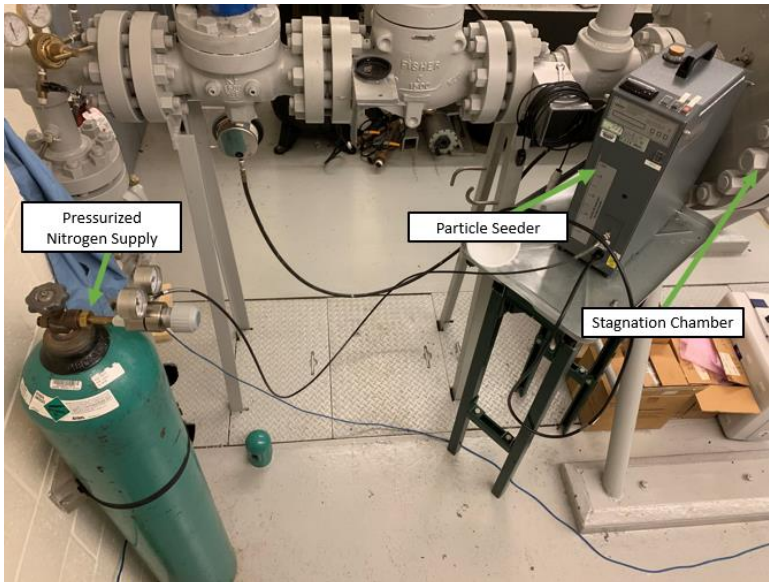

Fig. 16: ViCount Mineral Oil Seeder System

2.4 Quantel Evergreen PIV Laser

A Quantel Evergreen 532 nm double-pulsed Nd: YAG Laser is used as the light source. The laser beam is reflected into the test section of the tunnel from the bottom through a cylindrical lens expanding the beam into a sheet 1.5 mm thick as shown in figure 17. The laser is operated at the maximum output energy of 200 mJ/pulse. The repetition rate of the laser is 15 Hz; however, the two beams are timed with an offset of 0.5 μs. The operational parameters of the laser are listed in table 2.

Table 2: Laser Parameters

Wavelength	532 nm
Repetition rate	15 Hz
Pulse Offset	0.5 μs
Energy	200 ${}^{mJ}/_{pulse}$
Laser Sheet Thickness	1.5 mm

2.5 Optical path and beam alignment

In this experiment, SPIV measurements were taken at three spanwise locations in the flow. To accommodate changes in the location of laser sheet, the last three optical instruments including the cylindrical lens are mounted on traverses. These traverses allow for precise adjustments in the direction they are oriented, up to 0.5 inches from the center position. The full optical path is shown in figure 17.

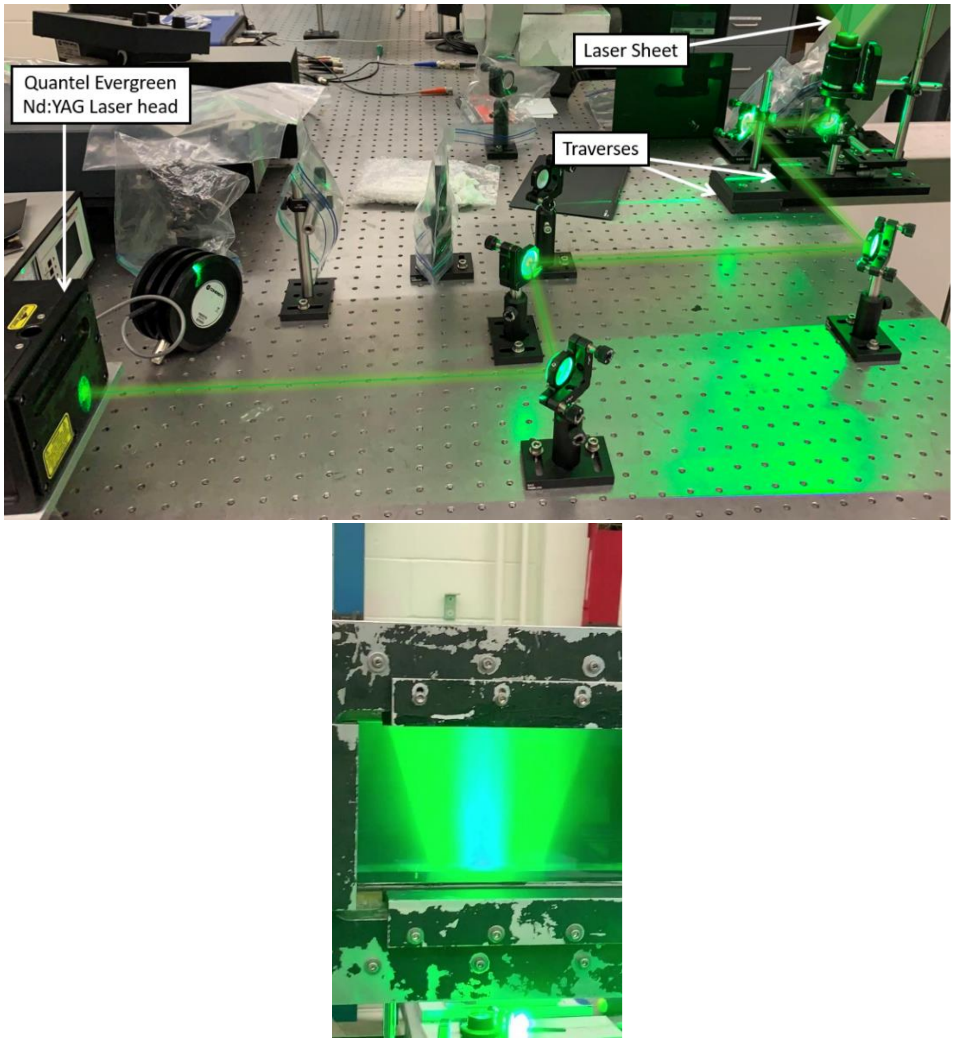

Fig. 17: Laser Beam Optical Path and Expanded Laser Sheet

For this experiment the sheet is aligned parallel to the freestream flow direction. The laser sheet is focused such that the thickness of the sheet in the area of interest is 1.5 mm. Using burn paper, we can image the laser sheet thickness and measure the burn directly. The focus is adjusted until the optimal thickness is achieved.

2.6 Cameras and Timing

Two LaVision sCmos Imager cameras fitted with 200 mm Nikon macro lenses are used to image the seed particles in the flow. The spatial resolution of the cameras is $20\frac{\mu m}{pixel}$. For SPIV, the cameras are not positioned perpendicular to the walls of the tunnel and as a result they are not perpendicular to the object plane. To resolve this, scheimpflug adapters are implemented between the cameras and the lenses. These adapters allow for the lenses to be set at an angle with respect to the camera sensors. At the right angle this can put the object plane perfectly in focus.

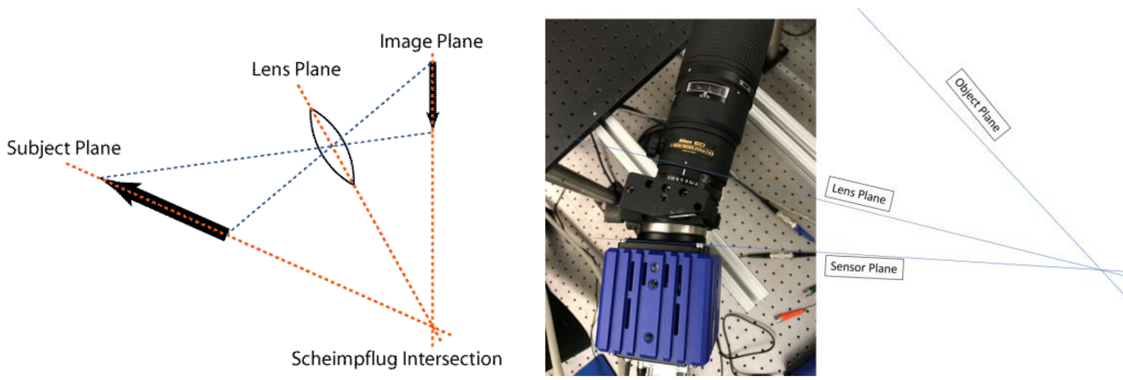

Fig. 18: Scheimpflug Principle

The cameras and laser are triggered externally using a Stanford Research Systems DG-535 digital delay generator. The maximum frame rate on these cameras is insufficient to record a set of images within the offset time between laser pulses, $0.5\mu s$. It is therefore necessary to time the laser pulses with the end and beginning of successive camera exposures in order to take a set of 2 images which are 0.5 μs apart. The timing of the system is illustrated in figure 19.

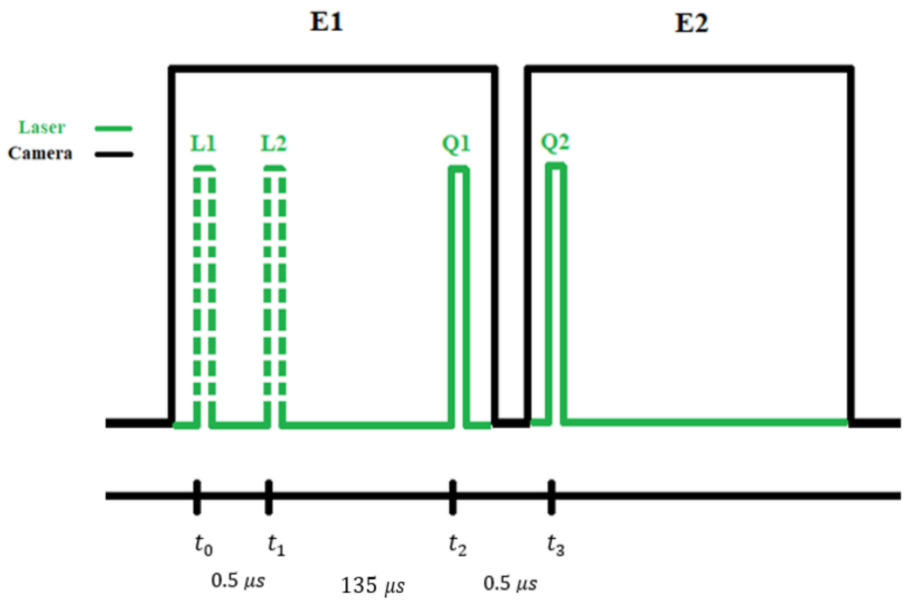

Fig. 19: Camera and Laser Timing

The cameras are triggered to expose at a rate of 15 Hz. For each set of images taken, the duration of the first and second exposures are referred to as E1 and E2 respectively. The flash lamp for the first laser, L1, is triggered at some time t_0 which is some time during the first exposure, E1. The Q- switch for the first laser, Q1, is triggered 135 μs after t_0, at a time t_2, which releases a laser pulse during the first camera exposure. The flash lamp for the second laser, L2, is triggered 0.5 μs after t_0, at a time t_1. The Q-switch for the second laser, Q2, is then triggered 135 μs after t_1, at a time t_3. The delay between flash lamp and Q-switch is adjusted such that the first laser pulse is entirely captured in the first exposure and the second laser pulse is entirely captured in the second exposure. By adjusting the timing of the cameras and laser system in this way, a set of images can be taken 0.5 μs apart. Through a single run of the experiment up to 300 sets of images can be taken in this way.

2.7 DaVis PIV Software

2.7.1 Calibration

In order to identify the angle of the cameras relative to the object plane and define a pixel to true length ratio, the software must be calibrated. A corrugated black plate with equally spaced white dots is used as a reference piece for the DaVis software. With the plate's front face aligned with the plane of interest for SPIV and in view of the cameras, the software can calculate the position and orientation of the cameras relative to the plane of interest; enabling the software to accurately calculate three velocity components.[16]

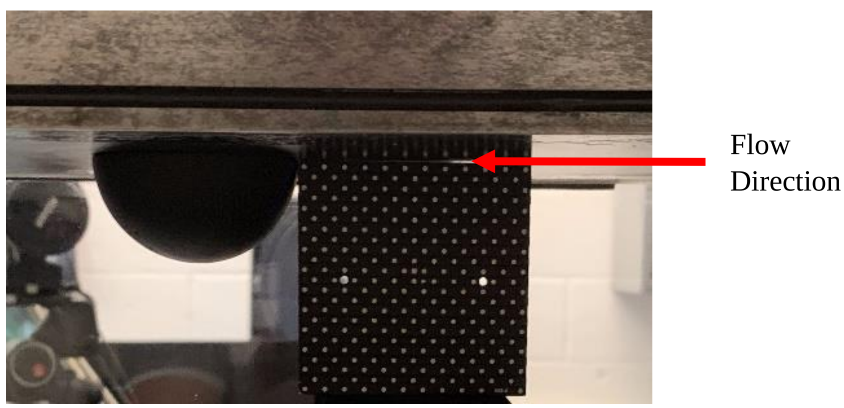

Fig. 20: Calibration Plate Location

2.7.2 Reflection Check

Depending on the geometry of the test model and the location of the cameras, specular reflections of laser light may enter the cameras. Generally, these reflections obscure the presence of seed particles in the flow. If the intensity of these reflections is high enough, the sensors on the cameras can be damaged. To avoid this, the intensity of light in view of the cameras is monitored through the DaVis program. If the intensity is found to exceed the allowable range for safe operation, then either the cameras are moved to new positions or the reflections are reduced. If the identified reflective surface can be painted or otherwise coated with an absorptive coating, the light reflected can be reduced. In this experiment the interior of the test section and the test model were painted black.

2.7.3 Image pre-processing

A sliding background subtraction is applied to the images to obtain a more uniform intensity distribution. Sharp intensity fluctuations from surface reflections can therefore be minimized. In this experiment the length scale for this process was 10 pixels, indicating the subtraction is calculated over areas of 10 x 10 pixels throughout each image.

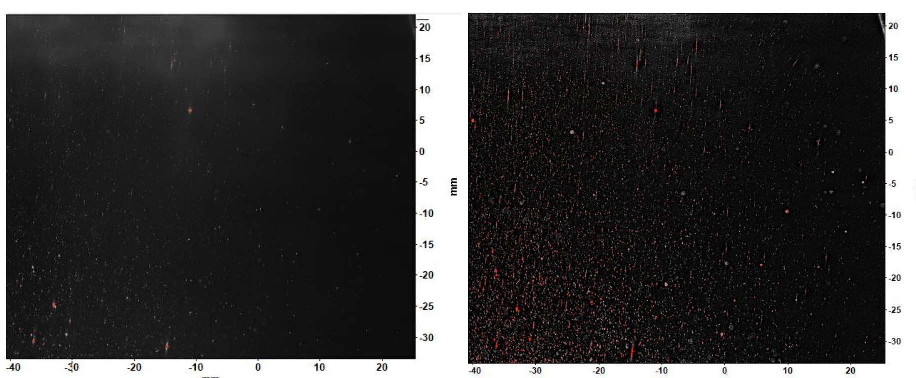

Before **After**

Fig. 21: Effect of Sliding Background Subtraction

Following this, the images are processed through a particle intensity normalization. In this process the software identifies the sliding minimum intensity, E_{min}, in a square area of a given length scale, in this case 5 pixels. The sliding minimum, E_{min}, is subtracted from the image yielding an image I_1.

$$I_0 - E_{min} = I_1 ; \quad I_0 \text{ is the original image}$$

The software then identifies the sliding maximum, E_{max}, in the same area as well as the maximum in an area with a length scale 10 times the original, E_{max10}. The final image, I_f, is obtained following the equation below.

$$I_f = I_1 \cdot \frac{Emax_{10}}{Emin}$$

This is useful to mitigate intensity fluctuations due to non-uniform particle diameter, which may lead to a bias error towards data from larger particles.[16]

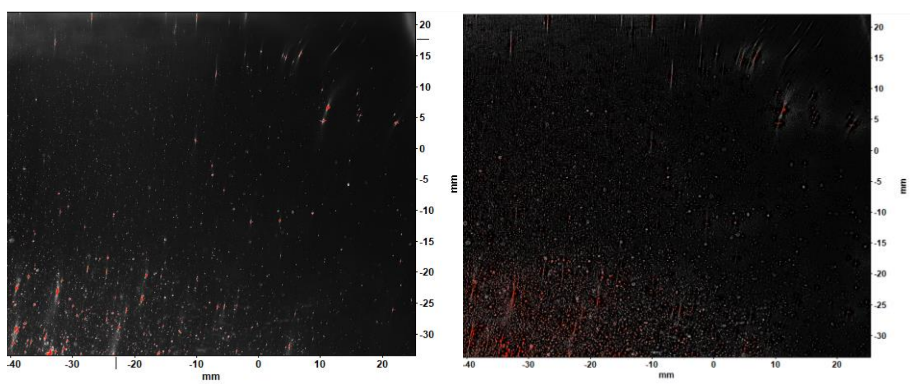

Before **After**

Fig. 22: Effect of Particle Intensity Normalization

2.7.4 Vector Calculation

As previously mentioned, DaVis uses a search algorithm to identify the direction and magnitude of velocity vectors by scanning for the shift which yields the highest cross-correlation value. In this experiment a multi-pass approach was used to improve the accuracy of the results. The vector field is calculated multiple times, iteratively refining the calculation by decreasing the interrogation window size and using the previously calculated vector as a starting point. The interrogation windows are shifted according to the reference vector field calculated in the previous pass. By doing so, the window shift is improved with each pass. This improves the accuracy and reliability of the vector field results by ensuring the same particles are visible in both frames even if small interrogation window sizes are used. This method also improves the signal-to-noise ratio.[16]

In this experiment the initial window size was 64x64 pixels and the final size was 48x48 pixels. A round (circular) Gaussian weighting function was applied. A 75% interrogation window overlap was applied. Overlap helps to adjust the resolution of the resulting vector field.

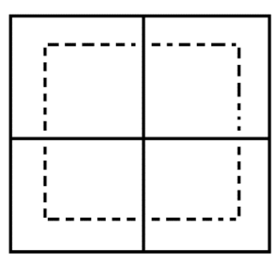

Fig. 23: Window Overlap Schematic

2.7.5 Post processing

As discussed in chapter 1, the ratio between the highest and second highest peaks in the cross-correlation search, the peak ratio, is a significant factor affecting the uncertainty of the results. In this experiment a minimum peak ratio of 1.1 was permitted and a median filter with universal outlier detection was applied.

A median filter compares a given vector to the median of a group of neighboring vectors in a neighborhood N. If the given vector is further from the median vector than the allowable deviation, then it is discarded. This vector may be replaced with one corresponding to the 2^{nd}, 3rd, or 4^{th} highest cross-correlation peaks if one of those peaks meets the median filter criteria. For the median filter criteria to be satisfied, all vector components must meet the criteria individually.

The universal outlier detection normalizes the median residual with respect to a robust estimate of the local velocity variation. The residual, r_i, is defined as the distance from one vector in N to the median of all vectors in N.[16]

$$r_i = |U_i - U_m|$$

$$r_0 = \frac{|U_0 - U_m|}{r_m}$$

U_0 is the vector under scrutiny, U_m is the median of the neighboring vectors of U_0, and r_m is the median of the residuals in N. A vector U_0 is removed if the residual, r_0 , is above the allowable limit.[16]

Chapter 3 Shock Wave Boundary Layer Interaction – Centerline

The purpose of this chapter is to present a novel data set of a flow field that had yet to be studied using PIV. We discuss the characterization of the flow field upstream and downstream of a wall mounted hemisphere, and the associated interaction of a three-dimensional bow shock with the turbulent boundary layer at the ceiling of the wind tunnel. The velocity at the spanwise centerline of the flow field was measured both upstream and downstream of a 38 mm radius hemisphere. The velocity at the spanwise centerline of the flow field was also measured upstream of a 25 mm radius hemisphere. We draw discussion from the comparison of these results with the available relevant literature [8, 9, 14, 20], and comment on the visible flow features and trends.

3.1 38 mm Centerline

In this section PIV data collected from the regions of interest upstream and downstream of a wall mounted 38 mm radius hemisphere is analyzed. Time averaged flow velocity components and turbulent quantities are discussed.

Figure 24 below shows velocity contours overlaid by schlieren photos from DeMauro et al [14] in which the same flow field was studied. The velocity is non-dimensionalized by the nominal freestream velocity, 640 m/s. The X and Y axes are scaled with the appropriate hemisphere radius, 38 mm. The origin represents a point at the same streamwise, X, location as the upstream edge of the hemisphere and 3mm vertically, Y, from the tunnel ceiling. PIV is sensitive to surface reflections. In this experiment surface reflections were present, particularly near the ceiling and hemisphere surface. Their effects are further discussed in this chapter.

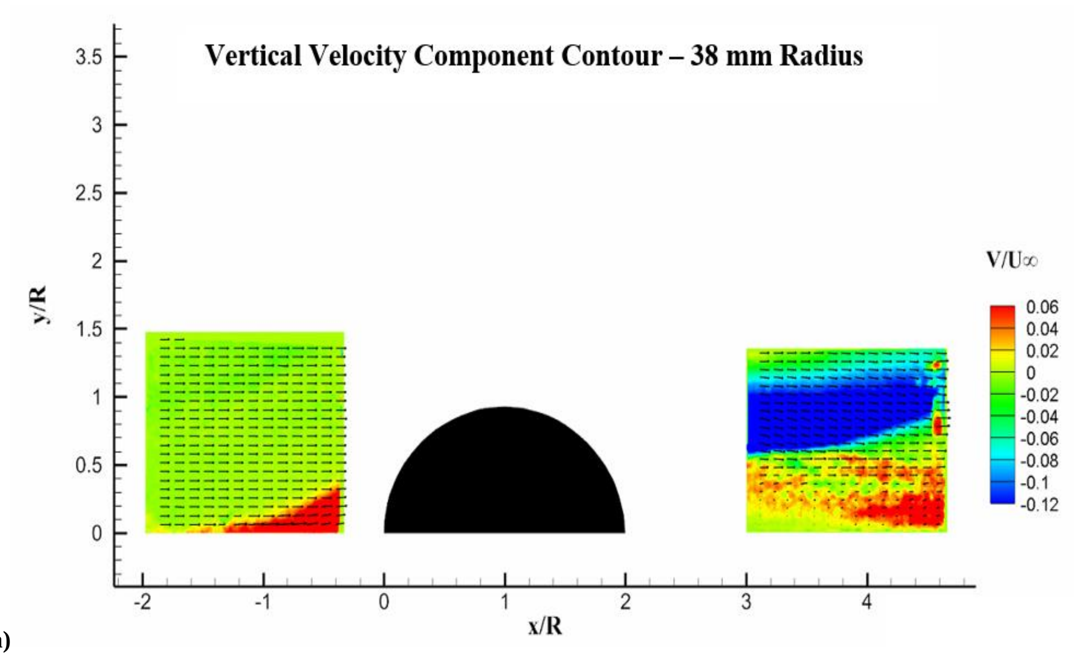

a)

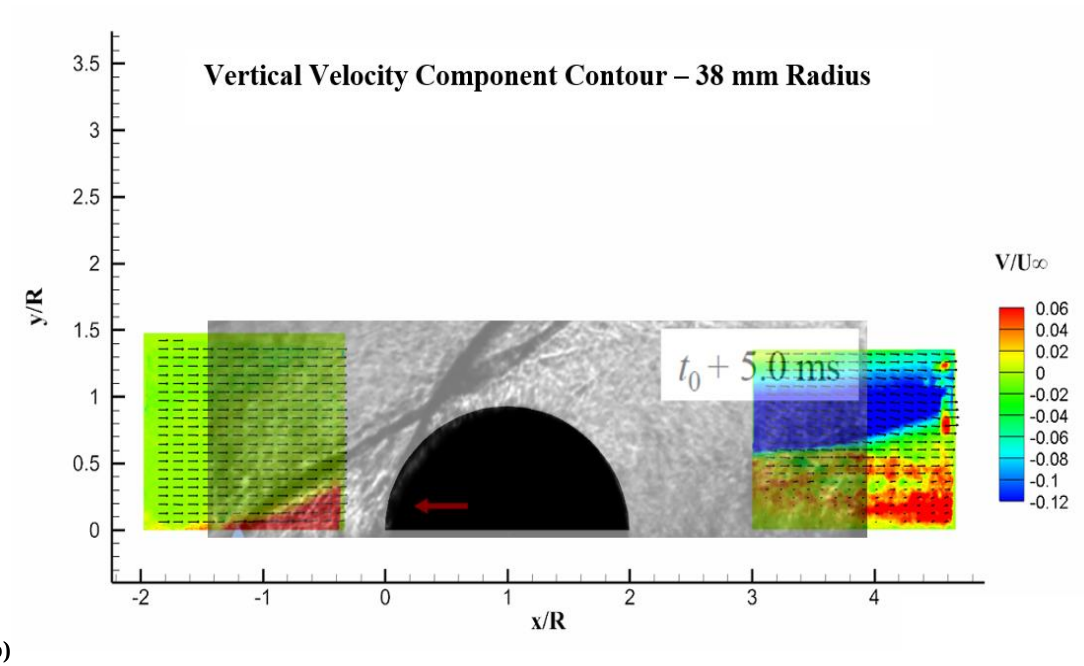

b)

Fig. 24 Vertical velocity contours with total velocity vector fields (a) overlaid with schlieren image from DeMauro et al [14] (b)

The velocity contour upstream of the hemisphere seen on the left side of fig.24 shows a strong upward turn of the flow coinciding with the separation shock wave. In the lower right corner of the contour the vertical velocity spikes. The boundary of this region where the vertical velocity jumps from 0 to over $0.06\ U_{\infty}$(~38 m/s) corresponds to the location of the separation shock wave. Furthermore, as seen in fig. 24 b, the apparent location of the shock coincides closely with schlieren images from DeMauro et al [14]. As we move downstream, the flow along the top surface of the hemisphere separates, and the separated shear layer continues into the wake. Evidence of the separated shear layer can be seen on the right side of fig. 24. The separated shear layer is also clearly visible in the schlieren image shown in fig. 25.

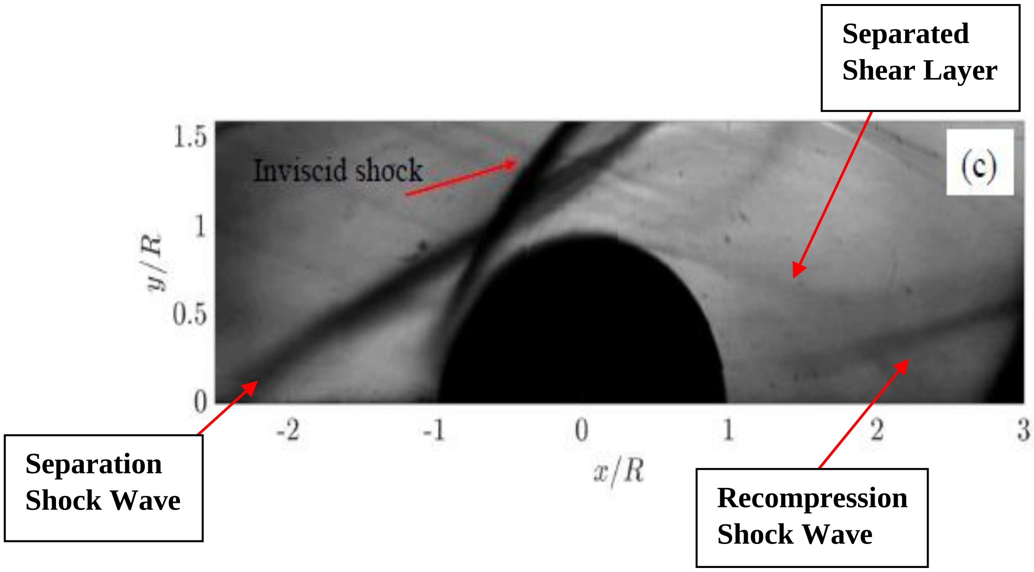

Fig. 25 Mach 3.4 hemisphere time averaged schlieren image from DeMauro et al [14].

Downstream, to the right of the hemisphere in fig. 24, we notice the flow velocity has a significant downward component above the separated shear layer. Below the shear layer as we move downstream, aft of the hemisphere, the flow begins to turn upward. This may be explained by a shock structure seen in the images by DeMauro et al [14]. More insight can be gleaned from the spanwise velocity contours shown below in fig. 26.

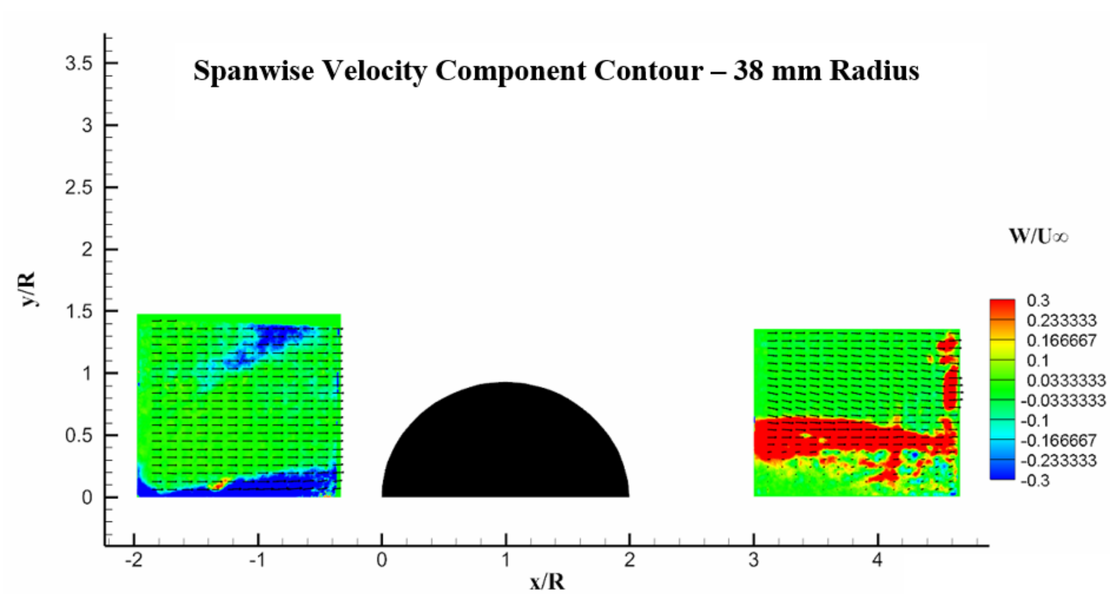

Fig. 26 Spanwise velocity contours with total velocity vector fields

The spanwise velocity field contour upstream of the hemisphere (left) shows almost no spanwise flow in most of the observed area. This is consistent with the expected centerline flow field. Areas in the upstream contour (left) that show non-zero spanwise velocity are localized where reflections were strongest and are likely the cause. Downstream (right), below the separated shear layer also shows a significant spanwise velocity for the downstream. While the effect of the reflections has not been quantified here, it is reasonable to assume them to be causing the inconsistencies upstream. This is further discussed in the section on spanwise trends. Alternatively, the presence of a spanwise flow near the upstream edge of the hemisphere could be evidence of turbulent eddies convected in the separation bubble.

Beresh et al [20] studied the wake of a hemisphere in supersonic flow at Mach 1.5 and 2.0. They observe flow in the wake moving away from the tunnel surface up toward the freestream and posit that the wake is comprised of two lobes with symmetry along the spanwise centerline in which "…the flow moves away from the wall near the centerline, moves laterally, and then returns to the wall off the centerline". Computational work by Morgan et al [8, 9] supports this claim. The wake measurements presented here do not contain data within 1 radius of the hemisphere (between X/R = 2-3) which that from Beresh et al [20] does, however we can make some insightful observations. The downstream spanwise velocity contour in fig 26. shows there is in fact a significant spanwise flow in this region. The streamwise velocity contours shown below in fig. 27 further this discussion.

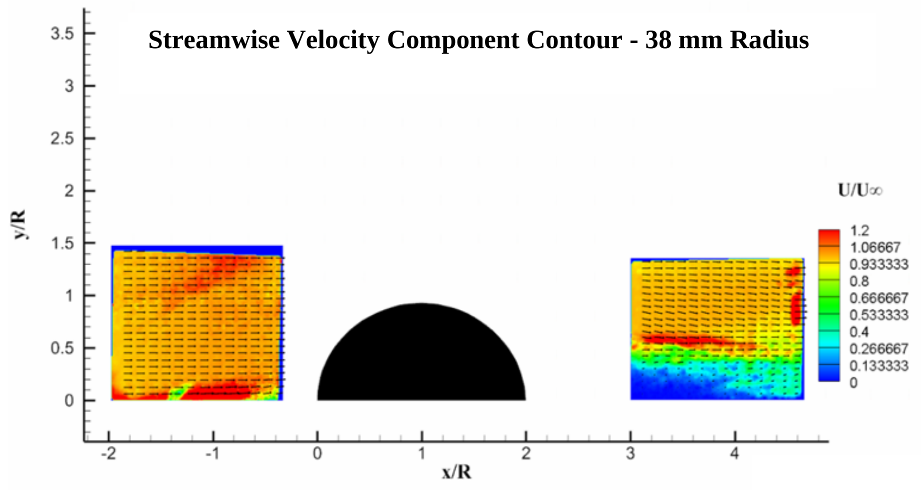

Fig. 27 Streamwise velocity contours with total velocity vector fields at Mach 3.4

Fig. 27 shows that downstream (right) of the hemisphere, a strong spanwise flow in the shear layer can be seen.

From the images provided by Beresh et al [20] we observe the separated shear layer lowering toward the tunnel surface and the recirculation region aft of the hemisphere retreating toward the hemisphere surface as Mach number increases. Selected results from Beresh et al [20] relevant for comparison are shown in fig. 7 presented in Chapter 1. While the recirculation region is not in view, we do observe a significantly lower separated shear layer at Mach 3.4. We also note a much less uniform wake in the shear layer; however, this may be influenced by surface reflections during PIV. A further understanding of the turbulence in this flow can be drawn from the turbulent kinetic energy contours shown below in fig. 28.

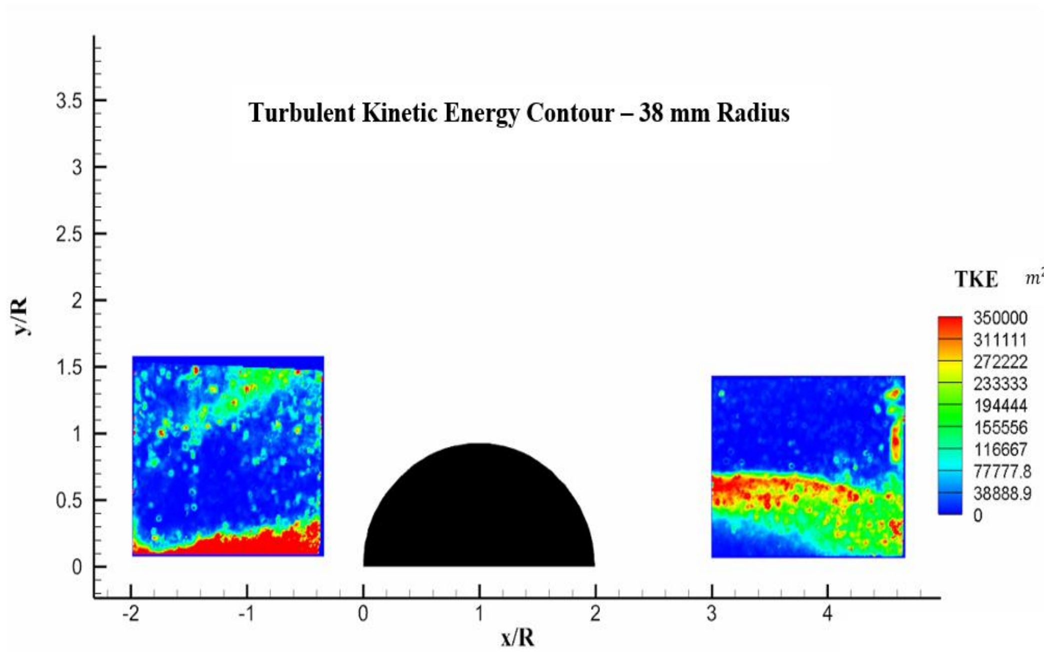

Fig.28 Turbulent kinetic energy contours

The turbulent kinetic energy, TKE, contours show the flow downstream (right) of the hemisphere is turbulent within the separated shear layer. In this region, the TKE decrease as the flow continues downstream and the turbulent eddies lose energy to viscous effects. The TKE contour upstream (left) of the hemisphere shows evidence of surface reflections in the same locations as the streamwise velocity contour in fig. 27. However, the spike in TKE immediately downstream of the shock foot location, ~ X/R = -1.4, may be indicative of the turbulent boundary layer separation. The low TKE value in the bulk of the freestream is consistent with the expected flow in this region. Measurements from the 25 mm radius shown below also show similar results.

3.2 25 mm Centerline

In this section PIV data collected upstream of a wall mounted 25 mm radius hemisphere is analyzed. Time averaged flow velocity components and turbulent quantities are discussed.

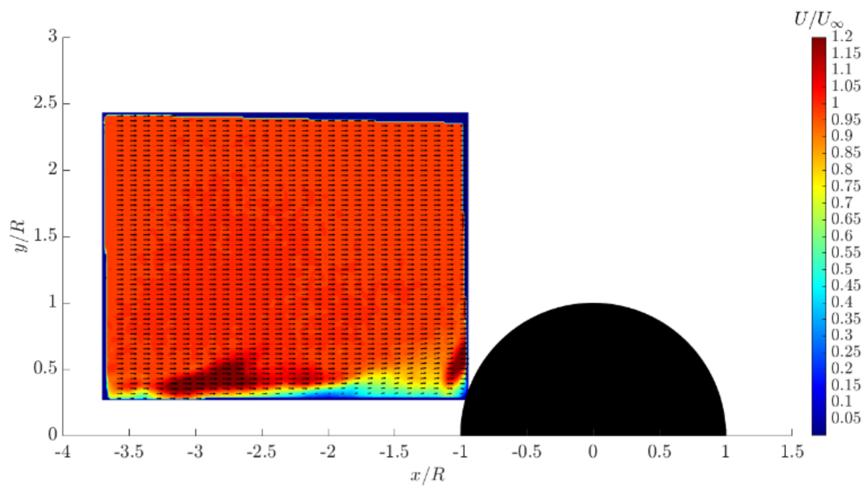

Fig. 29 Streamwise velocity contour with total velocity vector field, 25 mm radius

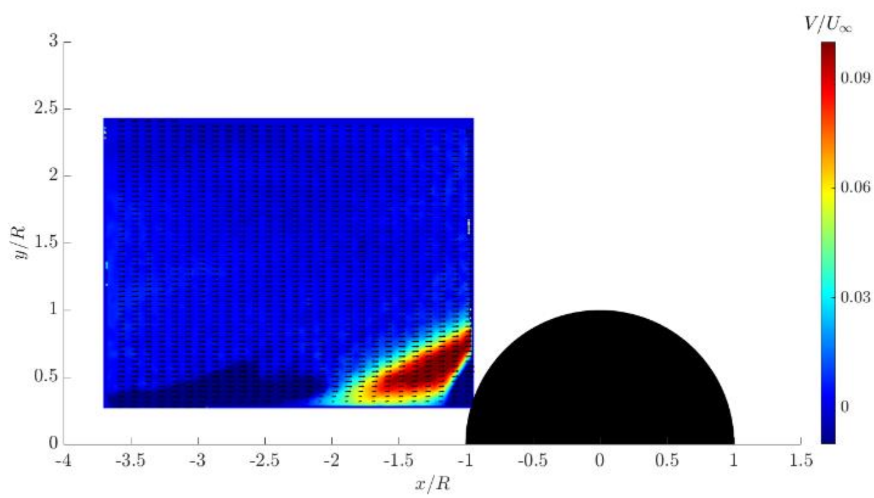

Fig. 30 Vertical velocity contour with total velocity vector field, 25 mm radius

As with the larger hemisphere we observe an upward turn of the flow coinciding with the separation shock wave. Fig. 30 shows a sharp increase in vertical velocity in the region near the hemisphere surface, $X/R \sim -2.2\ to -1$. Note, however, due to the proximity to the hemisphere body, reflections from the hemisphere obstructed data collection in the lower downstream corner of the contours (bottom right fig. 29 and fig. 30). These reflections are also seen in the spanwise velocity contour shown in fig. 31 below.

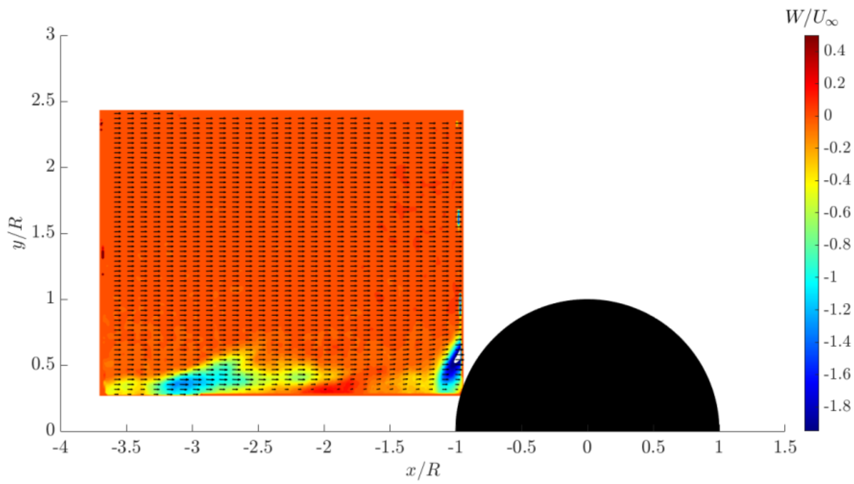

Fig. 31 Spanwise velocity contour with total velocity vector field, 25 mm radius

Fig. 31 shows the spanwise velocity contour upstream of the hemisphere. While most of the flow field shows zero spanwise flow upstream, there are some areas with non-zero values. As previously mentioned, while a non-zero spanwise velocity in this flow should not be present upstream of the hemisphere, it cannot be determined from this contour alone that surface reflections are responsible for the non-zero measurements. However, as compared to results from the other spanwise locations the high magnitude of the spanwise velocity and the total area of the non-zero region are much higher, implying reflections are the likely cause. This is expanded on when discussing spanwise trends in chapter 4. These effects persist in the turbulent kinetic energy, TKE, contour show in fig 32 below.

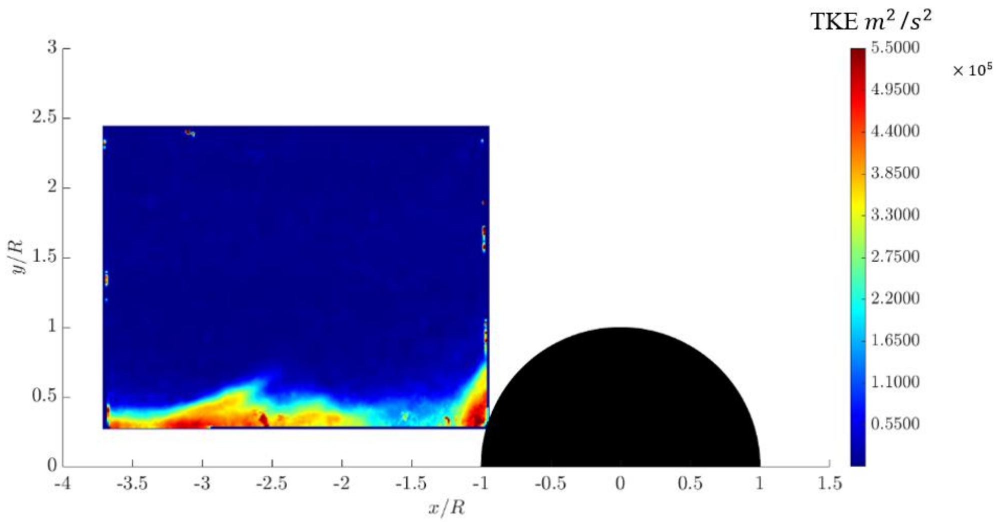

Fig. 32 Turbulent kinetic energy contour 25 mm radius

Fig. 32 shows turbulent kinetic energy, TKE, spikes along the bottom of the field in view, $Y/R \sim 0.28\ to - 0.6$, particularly near the hemisphere surface, $X/R \sim -1$. While high TKE immediately downstream of the separation shock foot, $X/R \sim -2.2$, could be indicative of the turbulent boundary layer separation, this contour shows evidence of surface reflections in the same locations as the velocity contours. Moreover, the TKE values near are much higher than can be expected, and the area of the non-zero region is very irregular. Both imply the presence of surface reflections. Low TKE values in the bulk of the freestream is consistent with the expected flow in this region.

Chapter 4 Shock Wave Boundary Layer Interaction – Spanwise Trends

The purpose of this chapter is to present a novel data set of a flow field that had yet to be studied using PIV. We discuss the characterization of the flow field upstream of a wall mounted hemisphere along three distinct spanwise planes, and the associated interaction of a three-dimensional bow shock with the turbulent boundary layer at the ceiling of the wind tunnel. The velocity at the spanwise centerline, 1.5 mm off center, and 3.0 mm off center of the flow field was measured upstream of a 25 mm radius hemisphere. We draw discussion from the visible flow features and trends. A measured estimate for the undisturbed boundary layer thickness of the test section ceiling of the Rutgers University Emil Buhler supersonic wind tunnel is also presented.

4.1 Undisturbed Boundary Layer

In this section PIV data collected upstream of a wall mounted 25 mm radius hemisphere are used to describe the undisturbed boundary layer thickness of the Rutgers University Emil Buhler supersonic wind tunnel. Data was collected at 3 spanwise locations: centerline, 1.5 mm off center, 3.0 mm off center. Fig 33 below shows a streamwise velocity contour at each of the three spanwise locations.

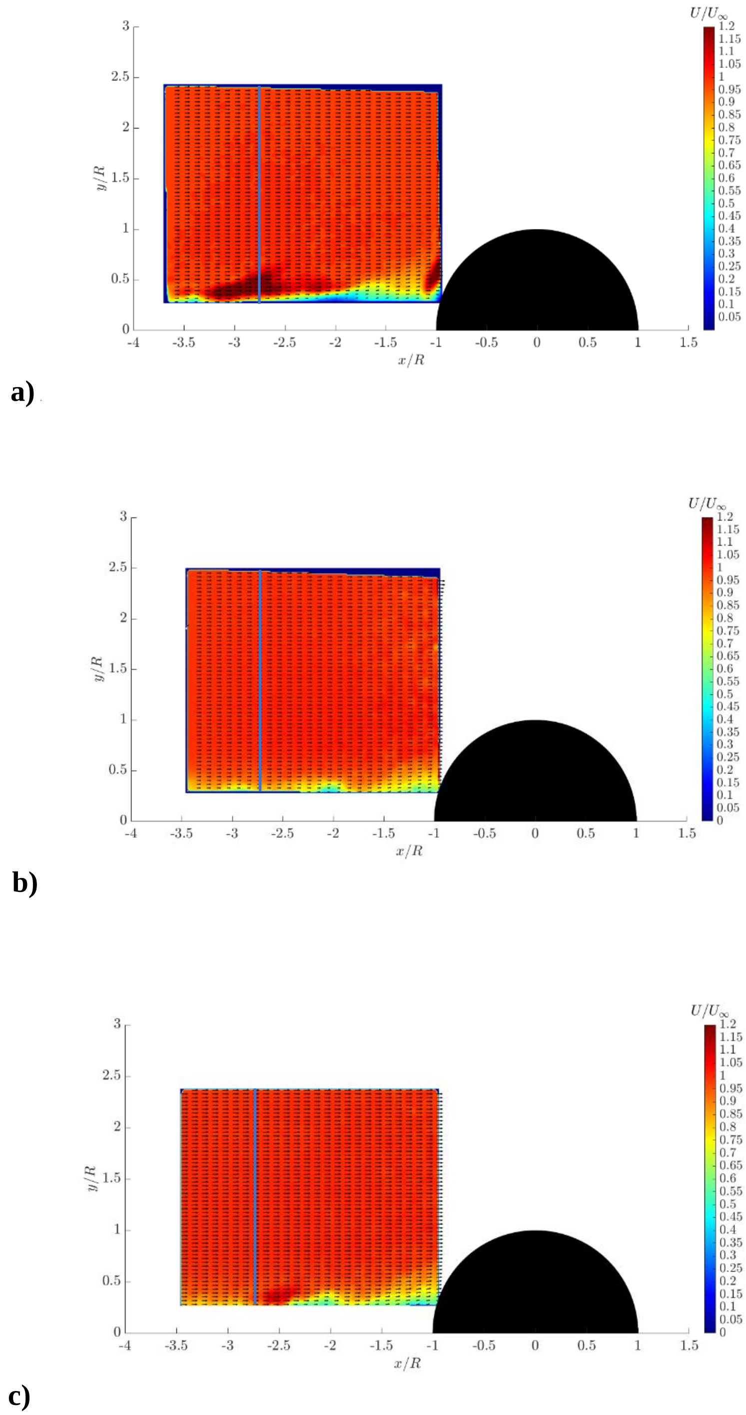

Fig. 33 Normalized streamwise velocity contours with total velocity vector field overlays at three spanwise locations centerline (a), 1.5 mm (b), and 3.0 mm off centerline (c). Vertical line indicates X/R = -3.25.

Upstream of the hemisphere, the tunnel ceiling generates a turbulent boundary layer. The boundary layer thickness, δ_{99}, is defined here as the vertical distance from the tunnel ceiling at which the streamwise flow velocity, U, reaches 99% of the freestream velocity, U_{∞}. This height at which the 99% U_{∞} value was reached was recorded at 10 streamwise locations upstream of the separation shock foot. This was repeated for each of the three spanwise measurements, totaling thirty δ_{99} measurements. These values were averaged to obtain the estimate presented here. Fig 34 below shows how the streamwise velocity changes as a function of vertical position at each spanwise location. The vertical blue line in fig. 33 corresponds to the streamwise location sampled in fig. 34, $X/R \sim -3.25$.

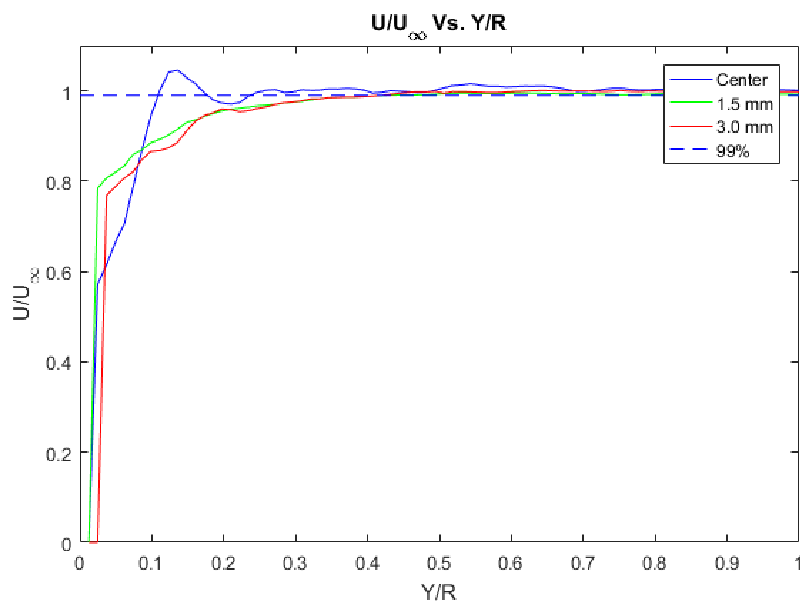

Fig. 34 Normalized streamwise velocity as a function of vertical position at X/R = -3.25

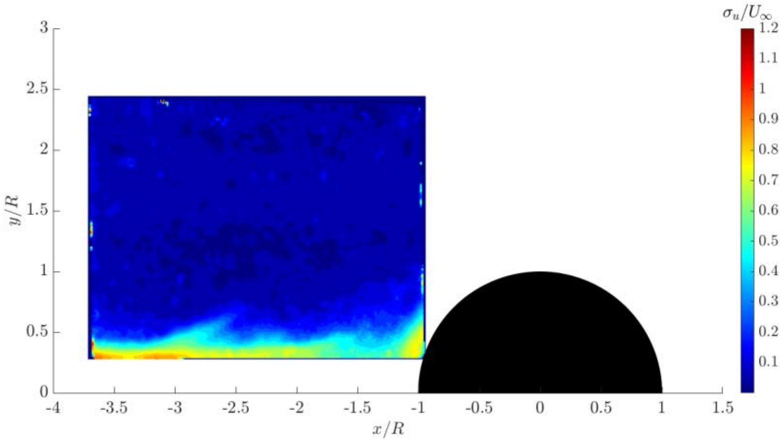
σ_u/U_∞
1.2
1.1
1
0.9
0.8
0.7
0.6
0.5
0.4
0.3
0.2
0.1
y/R
x/R
3
2.5
2
1.5
1
0.5
0
-4
-3.5
-3
-2.5
-2
-1.5
-1
-0.5
0
0.5
1
1.5

a)

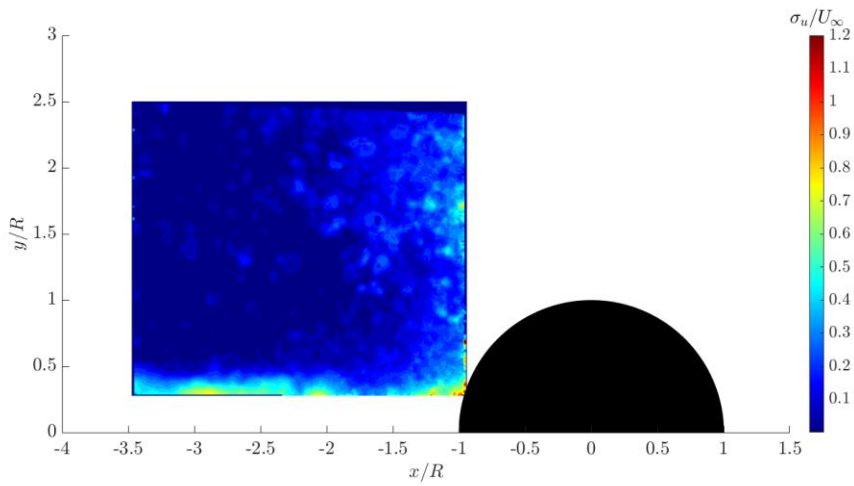
σ_u/U_∞
1.2
1.1
1
0.9
0.8
0.7
0.6
0.5
0.4
0.3
0.2
0.1
y/R
x/R
3
2.5
2
1.5
1
0.5
0
-4
-3.5
-3
-2.5
-2
-1.5
-1
-0.5
0
0.5
1
1.5

b)

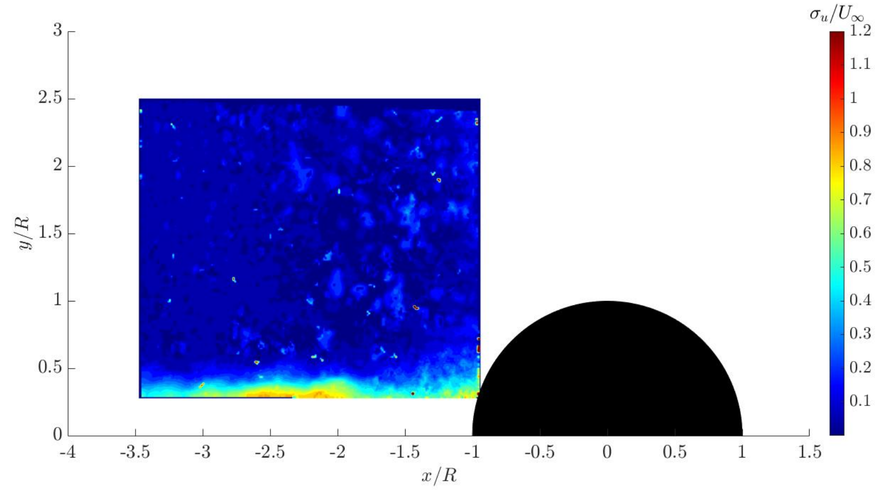

c)

Fig. 35 Normalized standard deviation of streamwise velocity contours at three spanwise locations centerline (a), 1.5 mm (b), and 3.0 mm off centerline (c)

As mentioned in chapter 1, the ratio of the hemisphere diameter to the undisturbed boundary layer thickness has been shown to carry little influence in the development of flow structures surrounding the hemisphere, however given the limited literature available, this quantity may prove important in the future and serves to give a complete overview of the tunnel parameters. Unfortunately, no previous boundary layer measurements were available for the tunnel ceiling in the test section. The collected data points for boundary layer thickness for each group were first compared to ensure there was no statistically significant difference between spanwise locations.

We expect that the boundary layer will not appear significantly different as we move spanwise. To check this, we apply a one-way analysis of variance, ANOVA. An ANOVA compares the variance of means among several data sets and determines if the variance is statistically significant.

SUMMARY

Groups	Count	Sum	Average	Variance
Center	10	203.3368	20.33368	7.235103
1.5	10	314.7444	31.47444	2.779156
3	10	301.7394	30.17394	13.75539

ANOVA

Source of Variation	SS	df	MS	F	P-value	F crit
Between Groups	742.1293	2	371.0647	46.83259	1.67E-09	3.354131
Within Groups	213.9268	27	7.923215			
Total	956.0561	29				

Table 3: Boundary layer measurement statistics: ANOVA

The F value among the groups was much larger than our critical value, 46.83 > 3.354 implying a significant difference. The confidence interval for this assessment is dictated by the P value. For a 95% confidence interval P must be less than 0.05, for 99%. Given P = 1.67E-09 < 0.05 the 95% confidence interval holds.

To determine where the difference came from, a series of Student's t-tests were conducted between each of the data sets. A Student's t-test considers two groups of data and determines if there is a significant difference in the means of the groups. For a two-tailed t test with 20 data points the critical value for a 95% confidence interval is t = 2.101. Which is to say a t value greater than 2.101 implies a significant difference in the data sets. The calculated t values for the comparisons of centerline with 1.5 mm off center and centerline with 3.0 mm off center were 6.792 and 11.13 respectively. These values are much higher than the critical value. When comparing the two off center data sets, we obtain a t value of 1.011 which is well below the critical value. We conclude the centerline data set is significantly different to the remaining data in terms of the boundary layer height definition. This is attributed to the bias created by surface reflections, which are more prevalent at the centerline. As a result, we omit the centerline data from our final boundary layer estimate. The final boundary layer estimate is the mean of the remaining data which gives a value of δ_{99} =16.52 mm $\pm$ 1.26 mm; where 1.95996 $\frac{\sigma}{\sqrt{n}}$ = 1.26 mm is the uncertainty associated the Student's t-test conducted for a confidence interval of 95%. .

4.2 Upstream Three-Dimensionality

In this section PIV data collected upstream of a wall mounted 25 mm radius hemisphere is analyzed. Data was collected at 3 spanwise locations: centerline, 1.5 mm off center, 3.0 mm off center. The three-dimensional flow features present are discussed as they appear in the spanwise trends in velocity, turbulent kinetic energy and Reynolds stresses.

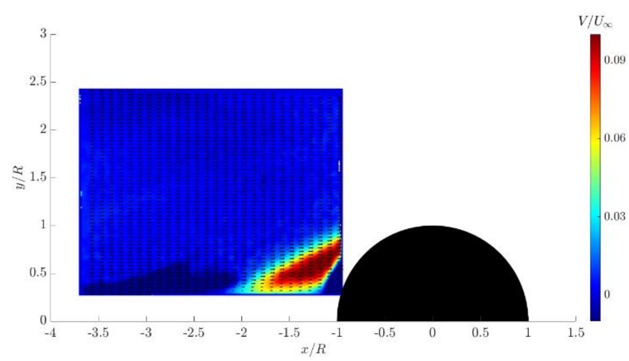

a)

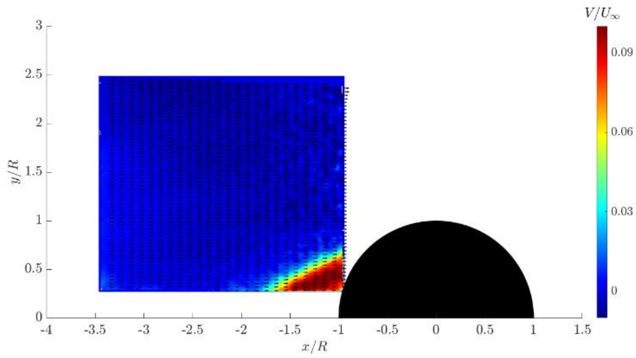

b)

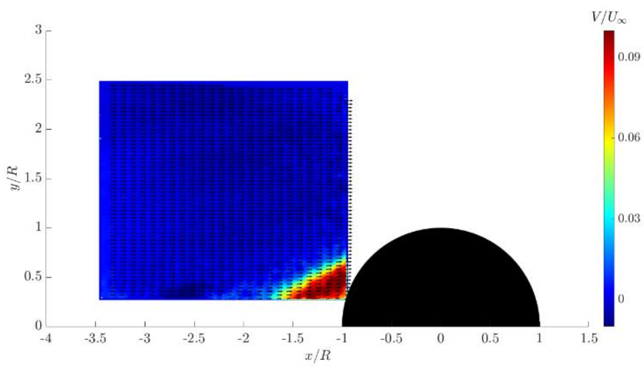

c)

Fig. 36 Normalized vertical velocity contours with total velocity vector field overlays at three spanwise locations centerline (a), 1.5 mm (b), and 3.0 mm off centerline (c)

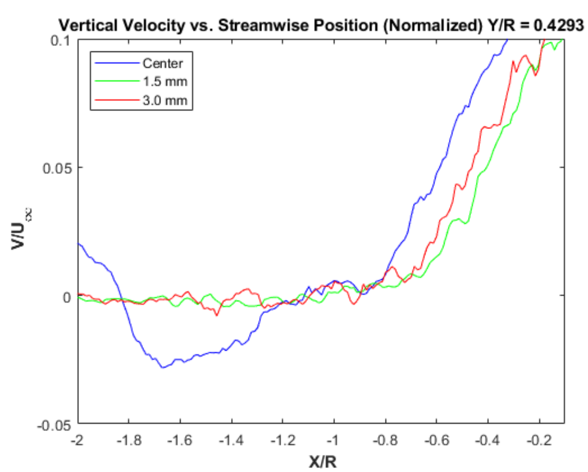

Fig. 37 Vertical velocity as a function of streamwise positon at Y/R = 0.4293

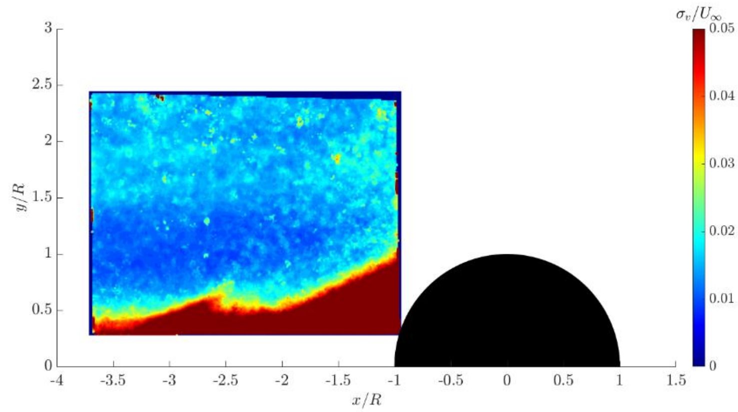

a)

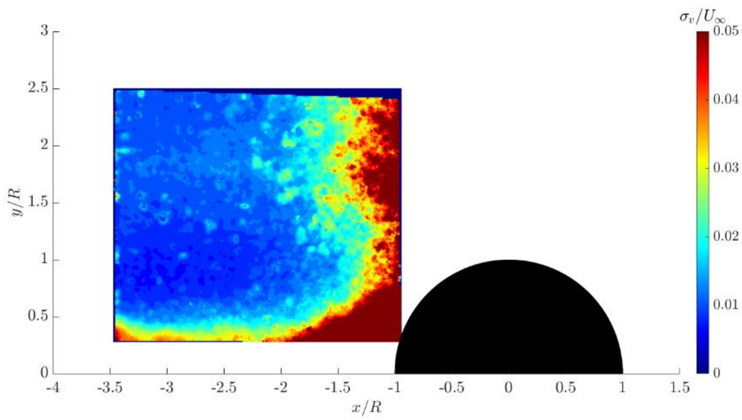

b)

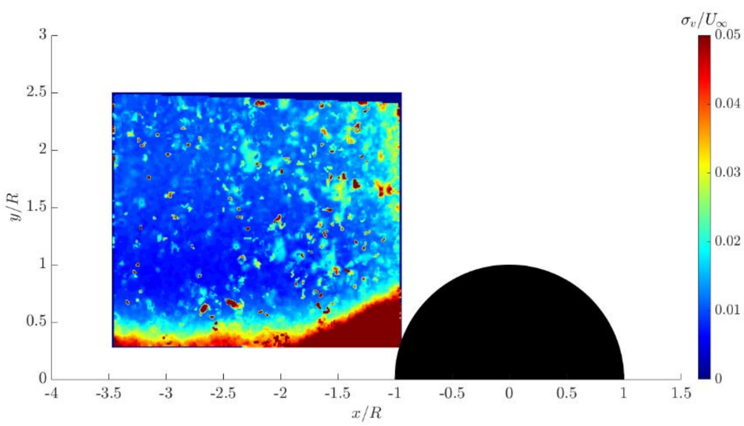

c)

Fig. 38 Normalized standard deviation of vertical velocity contours at three spanwise locations centerline (a), 1.5 mm (b), and 3.0 mm off centerline (c)

For the case of the 25mm radius hemisphere, three spanwise locations were studied. While we expect the onset of the separation shock to occur further downstream as we move spanwise, this trend is not clearly seen. This is likely due to the small distance, 1.5 mm, between planes and the differences falling into the noise. T

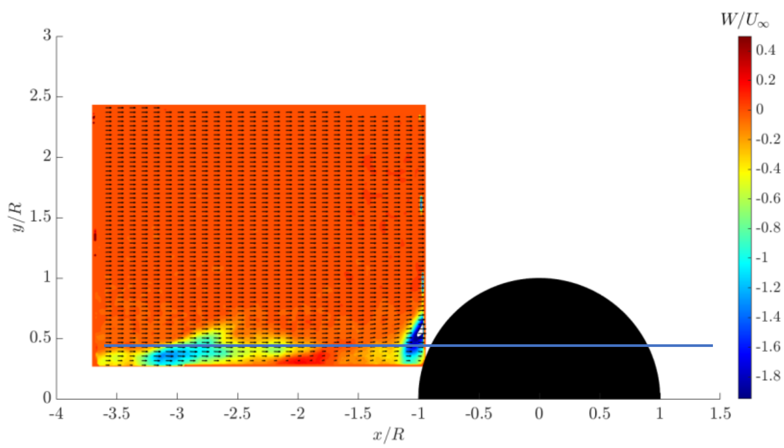

a)

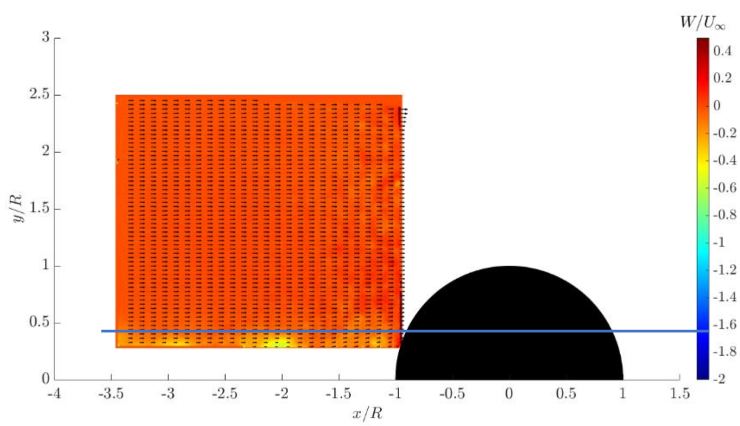

b)

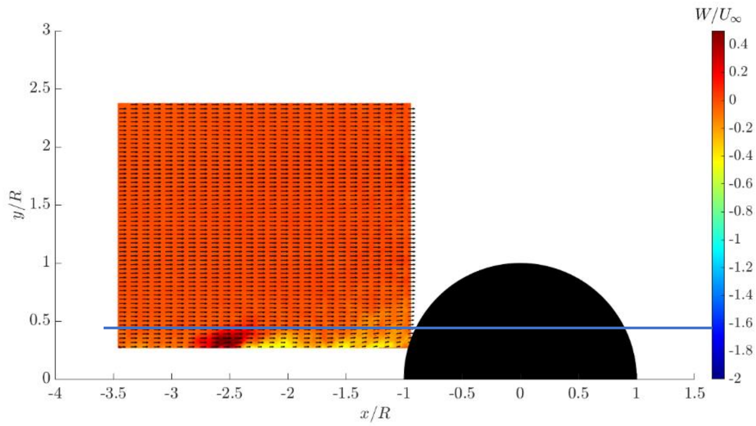

c)

Fig. 39 Normalized Spanwise velocity contours with total velocity vector field overlays at three spanwise locations centerline (a), 1.5 mm (b), and 3.0 mm off centerline (c). Horizontal line indicates Y/R = 0.4293.

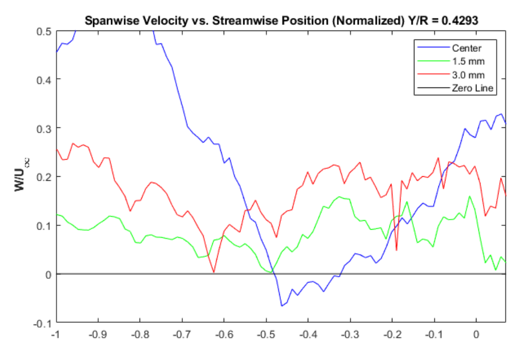

a) b)

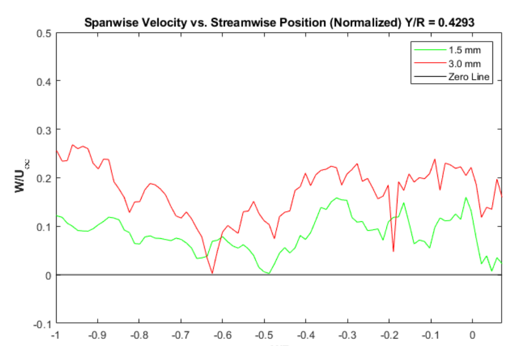

Fig. 40 Spanwise velocity as a function of streamwise position at Y/R = 0.4293 with centerline (a) and without (b)

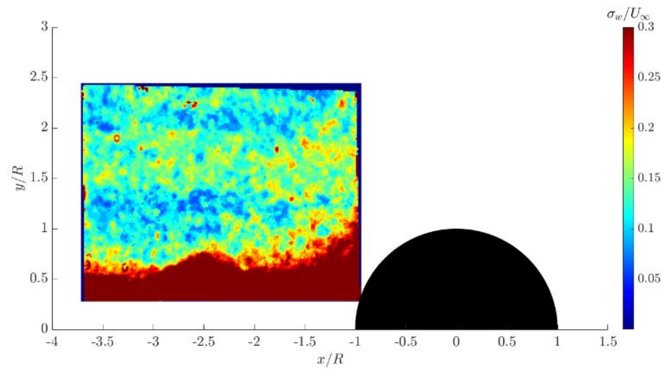

a)

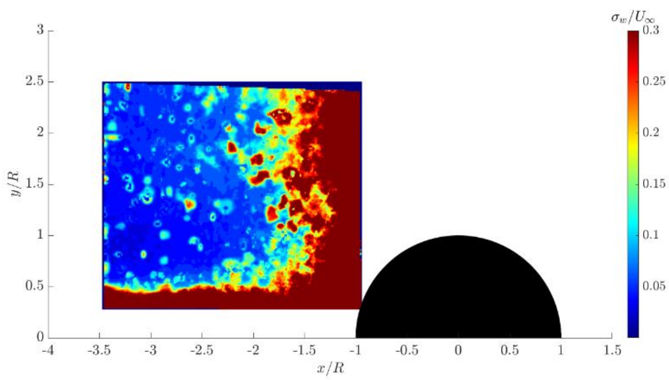

b)

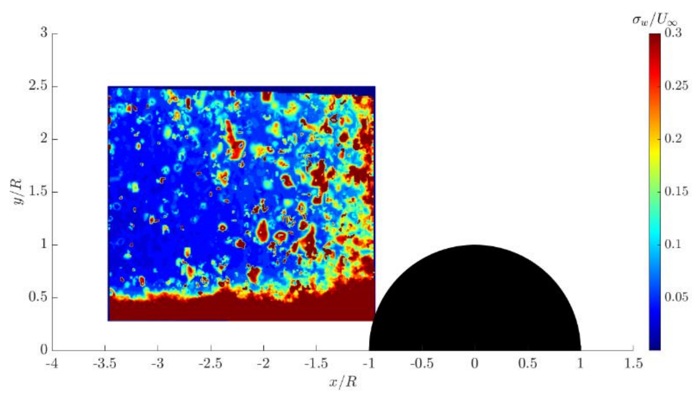

c)

Fig. 41 Normalized standard deviation of spanwise velocity contours at three spanwise locations centerline (a), 1.5 mm (b), and 3.0 mm off centerline (c)

The spanwise velocity data is quite noisy so any conclusions drawn are strictly conjecture that will have to be studied further in future work. That said, we make note of the apparent trends in the data with the knowledge that these trends are not definitive. The spanwise velocity is seen to increase as we move off center. As the flow navigates around the hemisphere it will move outward and over the surface. At the centerline there should be no outward motion and the flow should follow the centerline contour of the hemisphere. As we do observe a negative spanwise velocity component in the centerline case, the imaging plane may not have been perfectly aligned at the centerline. That said, the magnitude of the spanwise velocity is very high relative to off center measurements. At the centerline, reflections from the tunnel surface were more prominent than in off center cases, therefore we reason the spanwise velocity measured near the tunnel surface was likely influenced by these reflections.

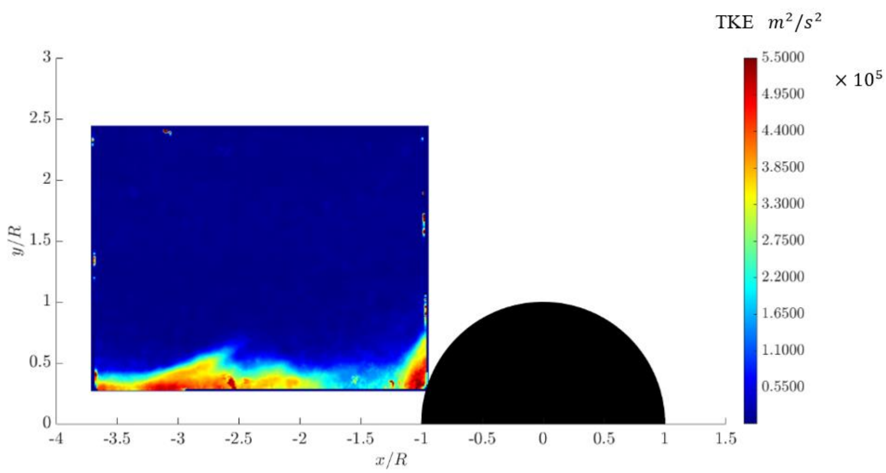

a)

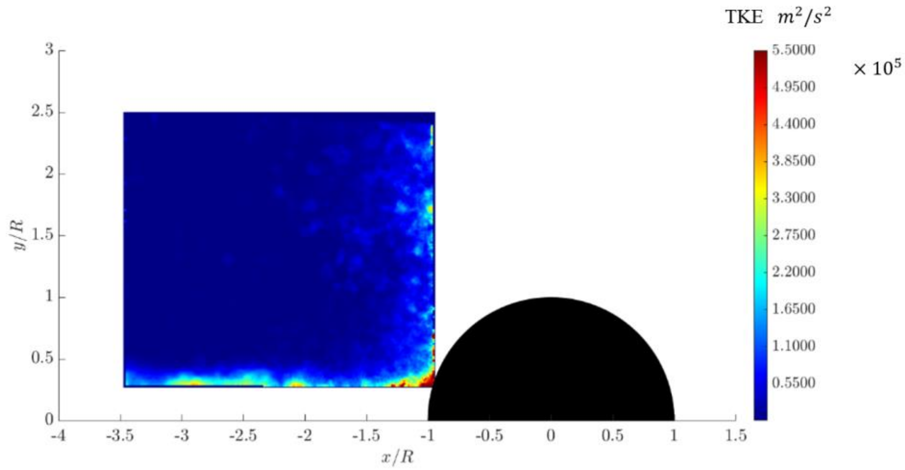

b)

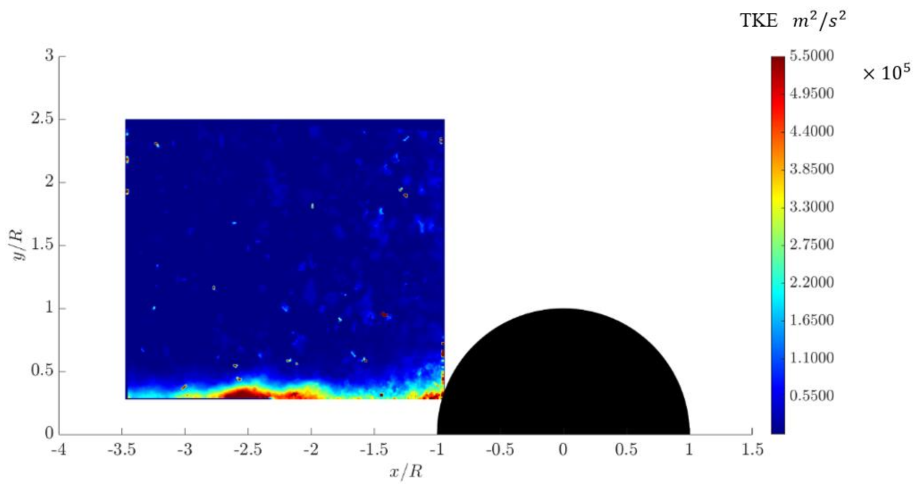

c)

Fig. 42 Turbulent kinetic energy contours at three spanwise locations centerline (a), 1.5 mm (b), and 3.0 mm off centerline(c)

The TKE contour for the centerline position shows sign of bias due to reflections. The off- center locations give a more accurate presentation of the TKE. It is important to note that we see a significant rise in TKE as we move further from the centerline. Similar quantities worth investigating are the Reynolds stresses. Reynolds stresses are the components of the total stress in a fluid attributed to the turbulent fluctuations in the fluid.

When a Reynolds decomposition is used, the flow velocity is defined as the sum of a mean flow velocity and a turbulent fluctuation.

$$u_i = \overline{u_i} + u_i{}'$$

Where $\overline{u_i}$ denotes the mean flow velocity and $u_i{}'$ denotes the velocity imparted by turbulent fluctuations. The Reynolds stresses are defined by the turbulent fluctuations as follows.

$$R_{ij} = \rho u_i{}' u_j{}'$$

The fluid density is ρ. In this experiment, the Reynolds stresses presented are normalized by the density.

$$R_{ij} = u_i{}' u_j{}'$$

The Reynolds stresses which include the fluctuations in the spanwise, z, direction are shown in the contours below in fig. 43 and 44.

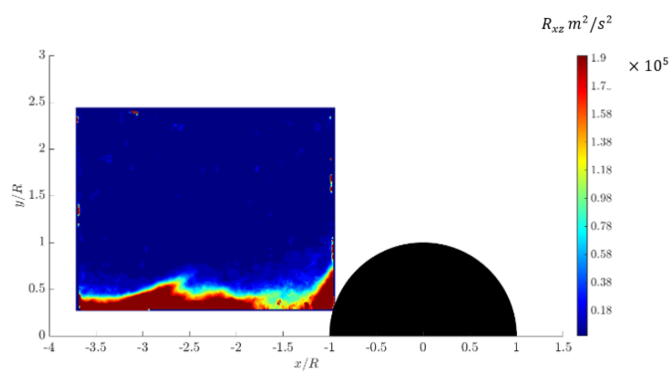

a)

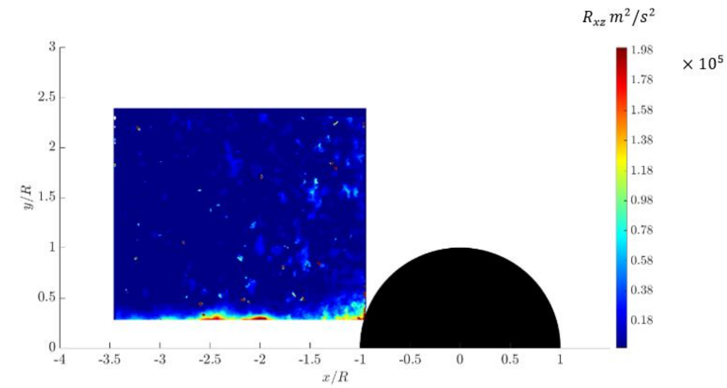

b)

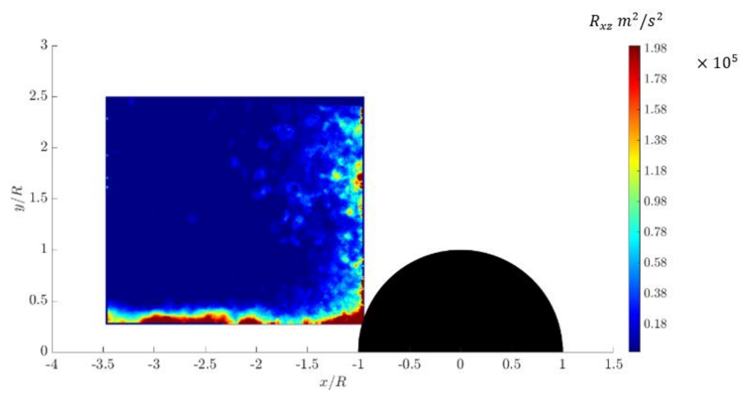

c)

Fig. 43 X-Z plane Reynolds stress contours at three spanwise locations centerline (a), 1.5 mm (b), and 3.0 mm off centerline (c)

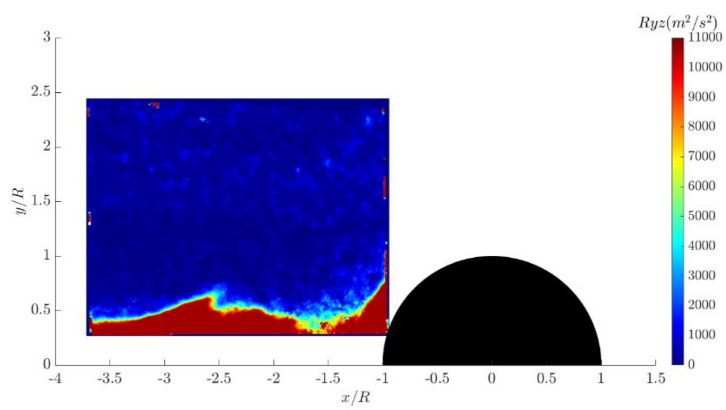

a)

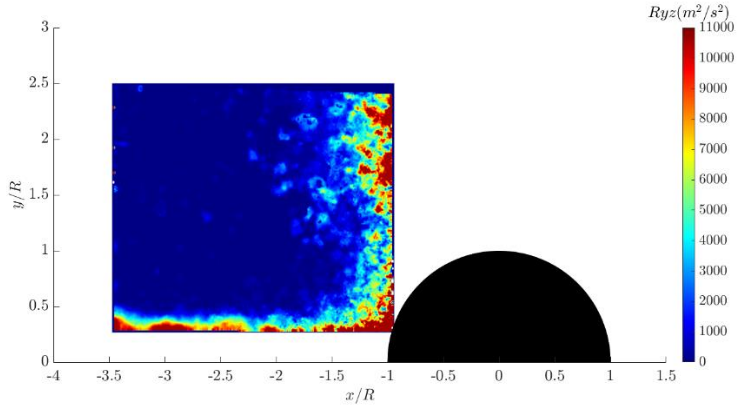

b)

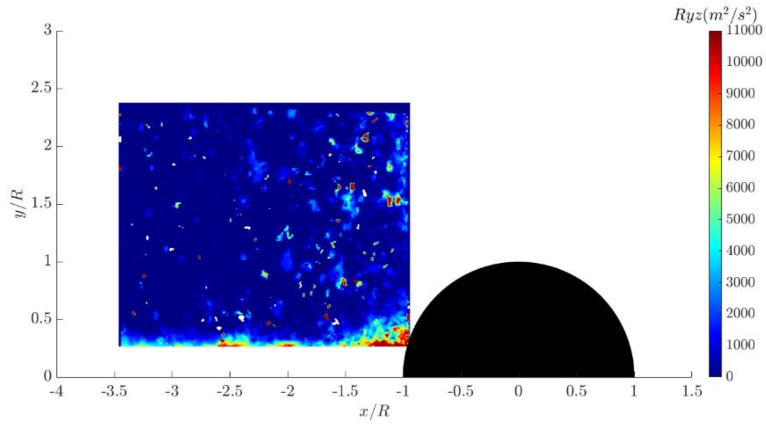

c)

Fig. 44 Y-Z plane Reynolds stress contours at three spanwise locations centerline (a), 1.5 mm (b), and 3.0 mm off centerline (c)

The Rxz and Ryz Reynolds stresses show the product of the turbulent fluctuations in the x and z directions. Accounting for the influence of reflections in the centerline case, we can see a steady increase in these quantities as we move spanwise from the centerline (from a to be to c). This is indicative of a three-dimensional flow consistent with what we expect from a hemispherical flow obstruction, the flow moving outward toward the tunnel walls.

As we move off center, fluctuations in the spanwise direction increase, implying that the flow experiences an increase in spanwise shear stress across the span of the hemisphere, in both the x-z and y-z planes. While this increase in shear stress is observed in the data, more work is needed to see if this trend extends beyond 3 mm off center. Nevertheless, the trend in the shear stress shows the flow is being turned toward the tunnel walls as it passes the hemisphere.

Chapter 5 Conclusion

5.1 Summary of Results

The supersonic flow around a wall mounted hemisphere at Mach 3.4 was investigated in the Rutgers University Emil Buhler supersonic wind tunnel using stereoscopic particle image velocimetry. Specifically, the flow upstream and downstream of a 38 mm radius hemisphere and the flow upstream of 25 mm radius hemisphere were studied. For the 38 mm radius hemisphere, quantities were measured along the spanwise centerline plane. For the 25 mm radius hemisphere, quantities were measured along 3 planes: spanwise centerline, 1.5 mm off center spanwise, and 3.0 mm off center spanwise.

The 38 mm radius hemisphere results showcase flow characteristics consistent with the available literature. The separation shock foot location lines up closely with the schlieren images from DeMauro et al [14]. As for the downstream flow field, we observe a significant spanwise flow which Beresh et al (2019) [20] postulated was likely present. Beresh et al [20] used planar particle image velocimetry and did not obtain any spanwise velocity data, however based on their results they speculated a significant spanwise flow was present downstream of the hemisphere. Here we confirm that there is a spanwise flow. Additionally, Beresh et al [20] studied this flow at two Mach numbers, 1.5 and 2.0. Their results show that the separated shear layer tends to shrink towards the tunnel wall as Mach number increased. Here we observe that this trend continues to 3.4.

Using data upstream of the separation shock foot, an estimate for the boundary layer thickness was calculated. 10 streamwise locations sampled for each of the three spanwise planes measured for the 25 mm radius hemisphere. Due to surface reflections the centerline data was biased and therefore removed from the estimate. The final estimate for the undisturbed boundary layer thickness of the wind tunnel ceiling was δ_{99} =16.52 mm $\pm$ 1.26 mm.

The 25 mm radius hemisphere results showcase some of the three-dimensionality of the upstream flow field. Specifically, we observe an increase in spanwise velocity w, and Reynolds stresses Rxz, and Ryz. The measurements of w are, however, not completely converged and therefore conclusions based on them must be marked for further study. These trends are consistent with the expected three-dimensionality upstream of the hemisphere, as well as the previous computational and experimental work in the literature.

5.2 Future Work

Future efforts should focus on three major areas: error mitigation, experimentation envelope widening, and measurement technique addition. In this study there were several identified sources of error, however, one notable and preventable source was surface reflections. This can be strongly mitigated using acrylic or other transparent materials for the hemisphere as well as the supporting section of the test section ceiling. Due to time constraints and material availability this option was not taken. While we do see the beginnings of spanwise trends in the results shown here, our findings are limited by the fact that only three planes spanning 3 mm, 12% of the radius, were studied. Moving forward, more planes spanning the entire hemisphere should be measured to fully quantify the flow field in three dimensions. The same can be said for the downstream wake as well. Lastly, while PIV is a useful tool, it is not the only one. A variety of measurement techniques can be applied to give a full picture of the flow as well as validating each other in areas where multiple methods are used. These methods can include but are not limited to pressure probes, pressure/temperature sensitive paints, and high speed quantitative schlieren imaging.

References

[1]Delery, J. and Marvin, J. G., "Shock wave/boundary layer interactions," AGARDograph N, Vol. 280, 1986.

[2]Gordeyev, S., Vorobiev, A., Jumper, E., Gogineni, S., and Wittich, D. J., "Studies of flow topology around hemisphere at transonic speeds using time-resolved oil flow visualization," AIAA Paper No. 2016-1459 , 2016.

[3]Beresh, S. J., Spillers, R. W., and Pruett, B. O. M., "Unsteady shock motion in a transonic flow over a wall-mounted hemisphere," AIAA J., Vol. 54, No. 11, 2016, pp. 3509–3515.

[4]Gordeyev, S. and Jumper, E., "Fluid dynamics and aero-optics of turrets," Prog. Aerosp. Sci., Vol. 46, No. 8, 2010, pp. 388–400.

[5]Danehy, P. M., Bathel, B., Ivey, C., Inman, J. A., and Jones, S. B., "NO PLIF study of hypersonic transition over a discrete hemispherical roughness element," AIAA Paper No. 2009-0394 , 2009

[6]Wang, D. P., Zhao, Y. X., Xia, Z. X., Wang, Q. H., and Huang, L. Y., "Experimental investigation of supersonic flow over a hemisphere," Chinese Science Bulletin, Vol. 57, No. 15, 2012, pp. 1765–1771.

[7]Bathel, B., Iyer, P., Danehy, P., Inman, J., Jones, S., Mahesh, K., and Johansen, C., "Comparing experiment and computation of hypersonic laminar boundary layers with isolated roughness," AIAA Paper No. 2014-0236 , 2014

[8]Morgan, P. E., Sherer, S. E., and Visbal, M. R., "Numerical exploration of supersonic flow over a wall-mounted hemisphere," AIAA Paper No. 2016-3650 , 2016.

[9]Morgan, P. E., Sherer, S. E., and Visbal, M. R., "Investigation of shock wave-boundary layer interaction for flow over a wall-mounted hemisphere," AIAA Paper No. 2017-3403 , 2017.

[10]Dolling, D. S., "Comparison of sharp and blunt fin-induced shock-wave/turbulent boundary layer interactions," AIAA J., Vol. 20, No. 10, 1982, pp. 1385–1391.

[11]Sedney, R. and Kitchens, C. W., "Separation ahead of protuberances in supersonic turbulent boundary-layers," AIAA J., Vol. 17, No. 6, 1979, pp. 579–585.

[12]Ojala, D. E., Characterization of shock wave turbulent boundary layer interaction using particle image velocimetry , Master's thesis, Rutgers, The State University of New Jersey, January 2012.

[13]Stroehle, E. J., The design and construction of a wind tunnel for education and research, Master's thesis, Rutgers, The State University of New Jersey, October 1999

[14]Demauro, E. P., Panco, R., Khamseh, A. P., & Chopra, A. (2018). High-Speed Schlieren Imaging of Supersonic Flow Past a Wall-Mounted Hemisphere With Turbulent Boundary Layer Impingement. 2018 *Fluid Dynamics Conference*

[15]Willert, C.E. & Gharib, Digital particle image velocimetry. *M. Experiments in Fluids* (1991)

[16]LaVision. (2016) DaVis v8.4 Product-Manual. Göttingen, Germany: LaVision GmbH.

[17]Urban, D.W., Mungal, M.G., "Planar Velocity Measurements in Compressible Mixing Layers," AIAA 97-0757, 35th Aerospace Sciences Meeting, Reno, NV, 1997

[18]Clemens, N. T. and Narayanaswamy, V., "Low-frequency unsteadiness of shock wave/turbulent boundary layer interactions," Annu. Rev. Fluid Mech., Vol. 46, 2014, pp. 469–492.

[19]Gaitonde, D. V., “Progress in shock wave/boundary layer interactions,” Prog. Aerosp. Sci., Vol. 72, 2015, pp. 80–99.

[20]Beresh, S.J., Henfling, J.F., Spillers, R. W. “Time-Resolved Planar Velocimetry of the Supersonic Wake of a Wall-Mounted Hemisphere” AIAA Journal, Vol 57, 2019, pp. 1383-1399

[21]Adrian, R. J., “Twenty Years of Particle Image Velocimetry” Experiments in Fluids, Vol 39, 2005, pp. 159-169

[22]Elsinga, G.E. , Scarano, F. , Wieneke, B. , van Oudheusden, B.W. , “Tomographic Particle Image Velocimetry” Experiments in Fluids, Vol 41, 2006, pp. 933-947

[23]Prasad, A.K. “Stereoscopic Particle Image Velocimetry” Experiments in Fluids, Vol 29, 2000, pp. 103-116

[24]Aderson, J.D. “Modern Compressible Flow with Historical Perspective”, McGraw-Hill Education, 2003

[25]Kundu, P.K., Cohen, I.M., Dowling, D.R. “Fluid Mechanics”, Elsevier, 2016

[26]Panco, R. and DeMauro, E.P.” Application of Stereoscopic Particle Image Velocimetry in the Rutgers Supersonic Wind Tunnel”, AIAA, 2019

[27] “Particle Image Velocimetry” *https://www.lavision.de/en/techniques/piv-ptv/.*

Appendix

Additional Graphs

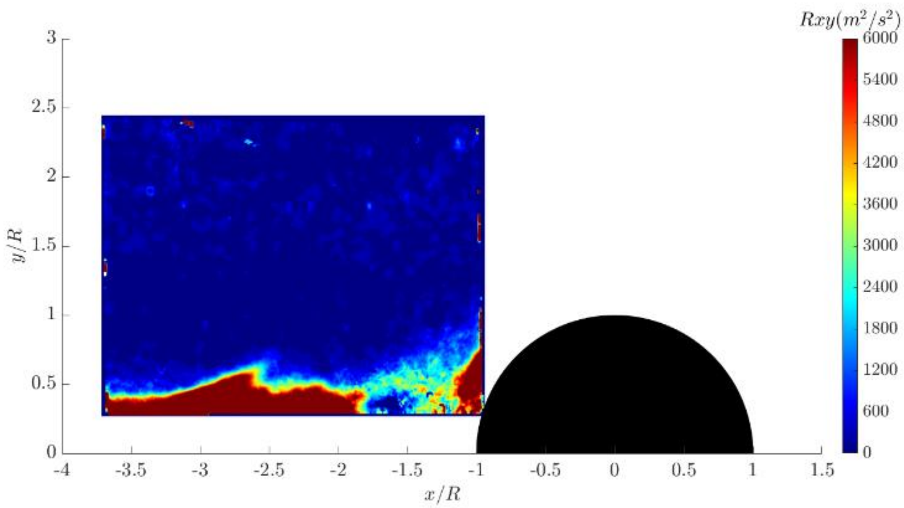

a)

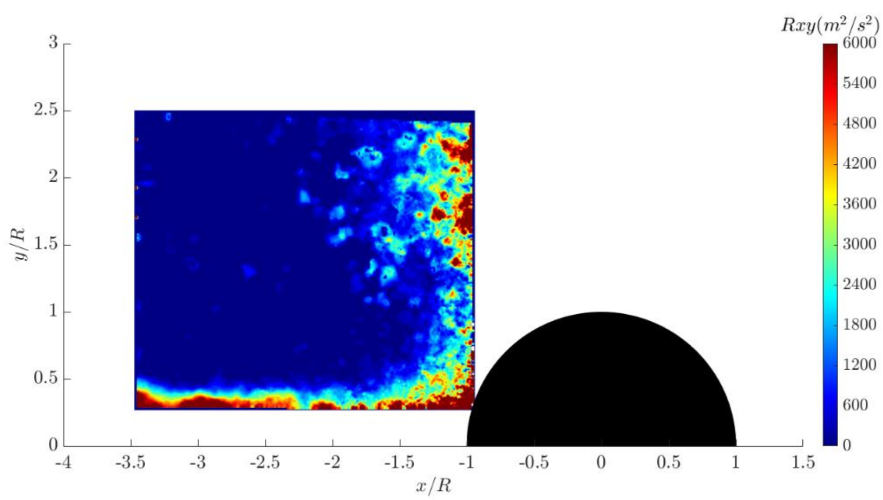

b)

c)

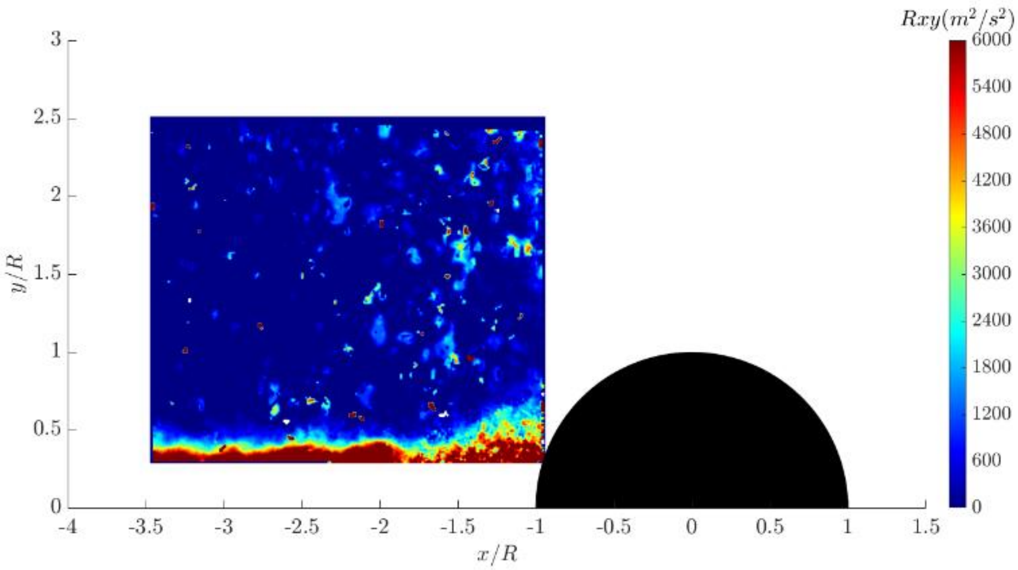

Fig. A1 Reynolds stress Rxy along three spanwise planes: centerline (a), 1.5 mm off center (b), 3.0 mm off center (c)

a)

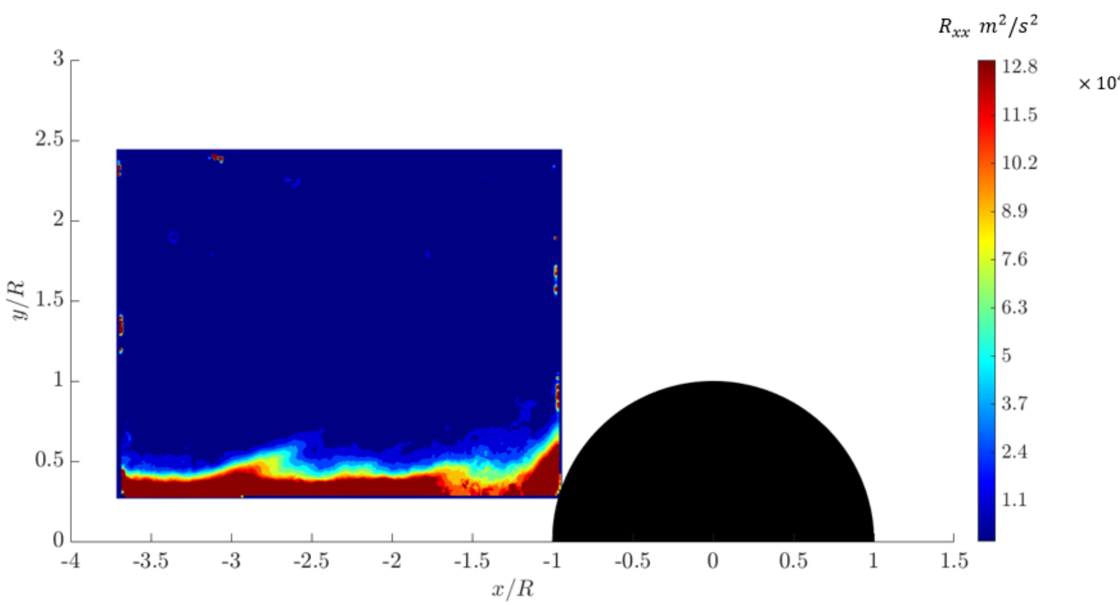

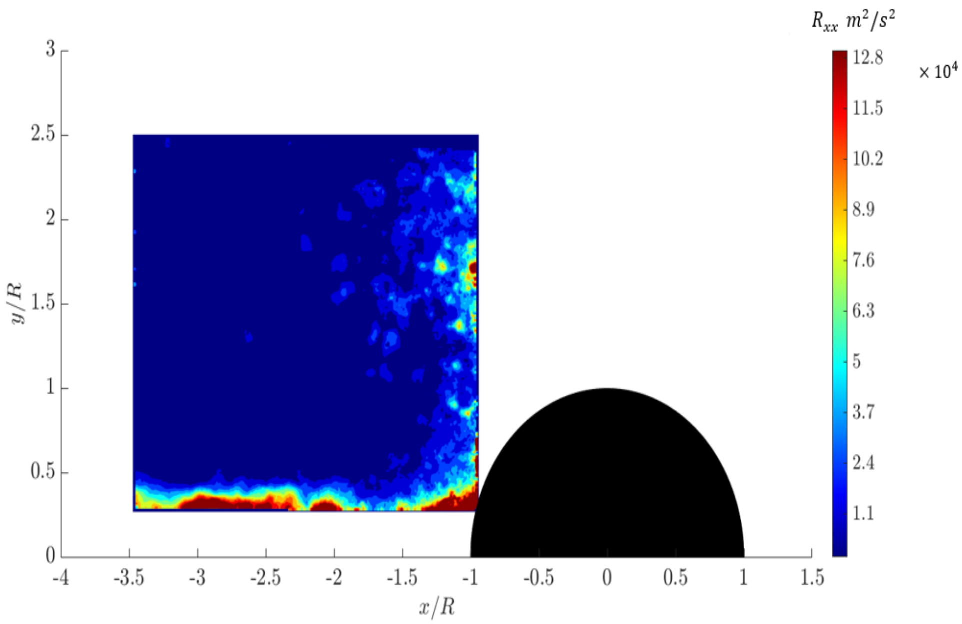

b)

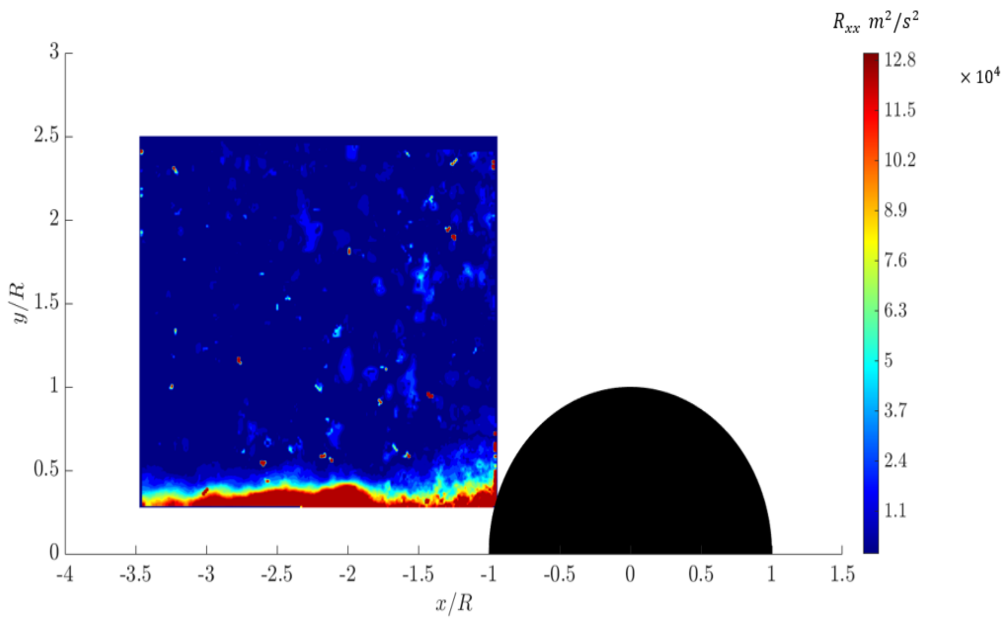

c)

Fig. A2 Reynolds stress Rxx along three spanwise planes: centerline (a), 1.5 mm off center (b), 3.0 mm off center (c)

a)

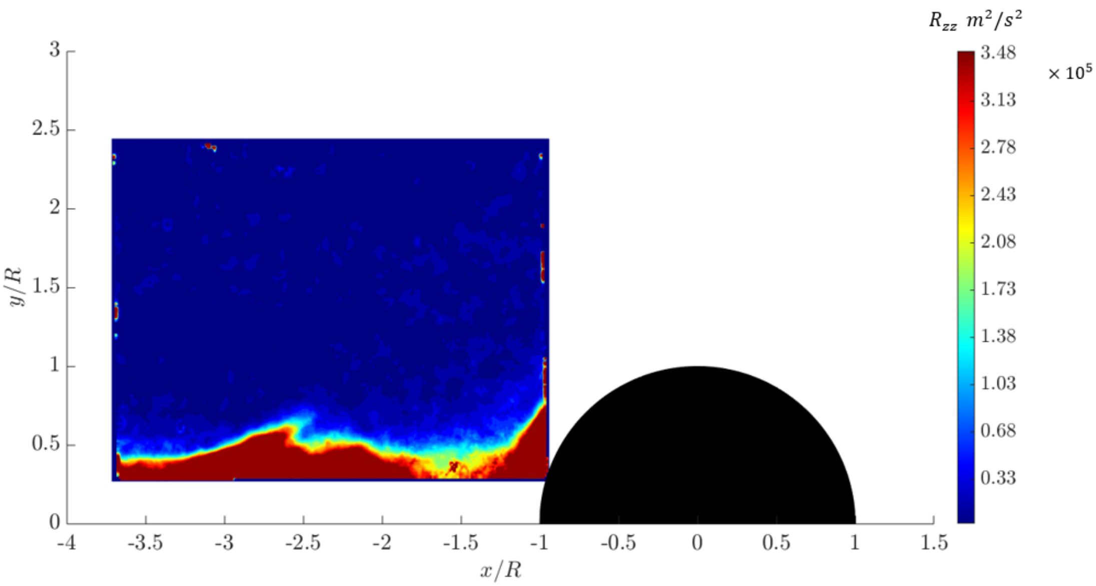

R_{zz} m^2/s^2
$\times 10^5$
3.48
3.13
2.78
2.43
2.08
1.73
1.38
1.03
0.68
0.33
y/R
x/R

b)

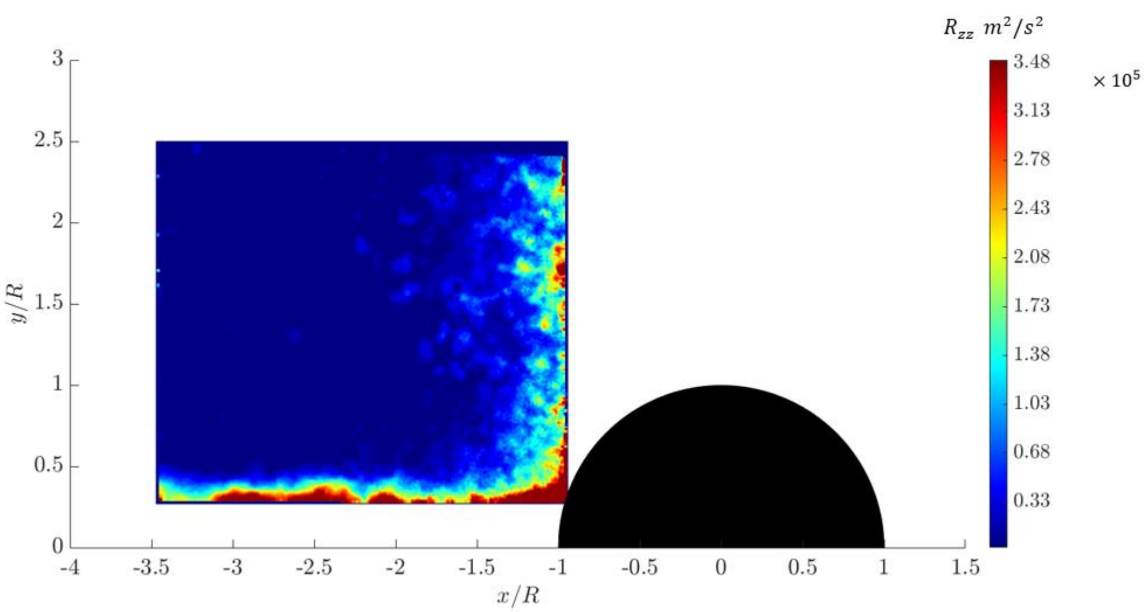

R_{zz} m^2/s^2
$\times 10^5$
3.48
3.13
2.78
2.43
2.08
1.73
1.38
1.03
0.68
0.33
y/R
x/R

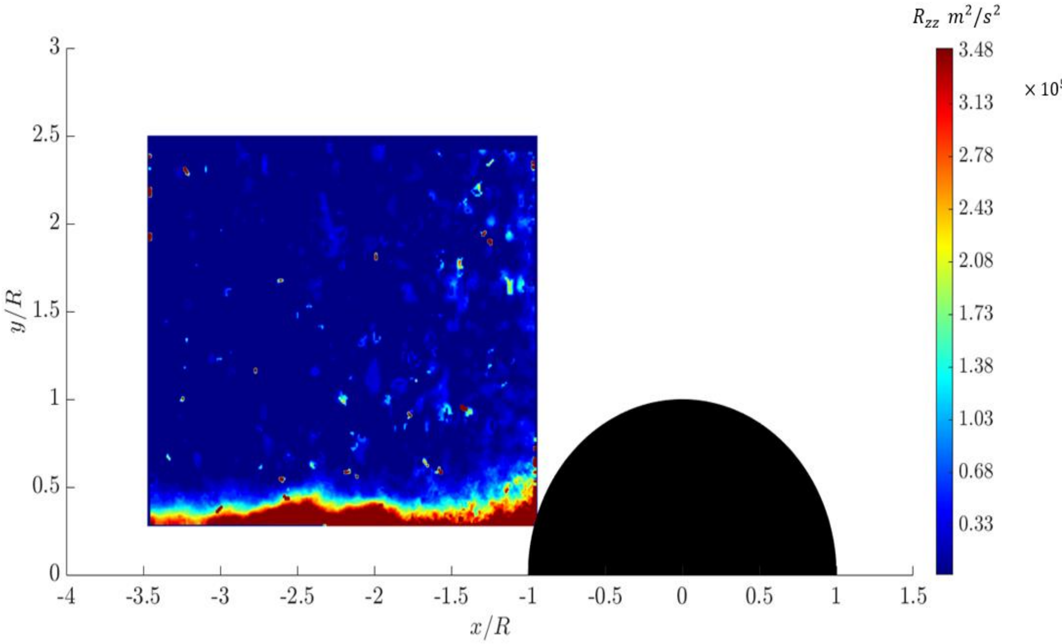

c)

Fig. A3 Reynolds stress Rzz along three spanwise planes: centerline (a), 1.5 mm off center (b), 3.0 mm off center (c)

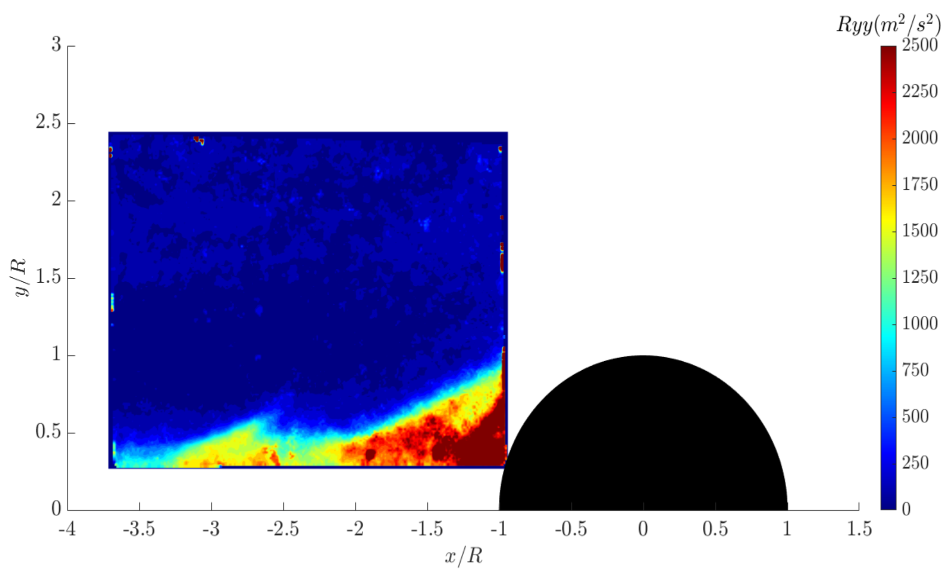

a)

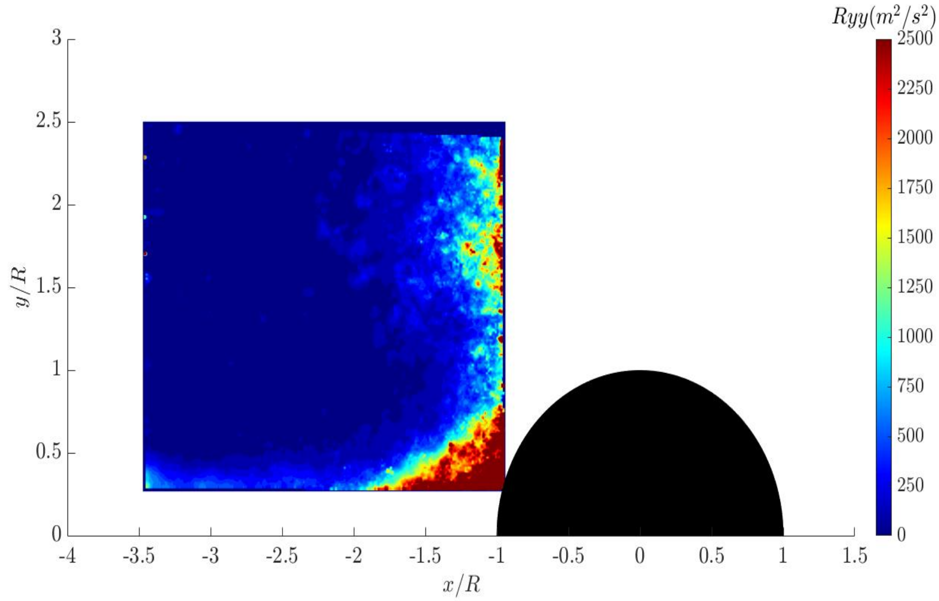

b)

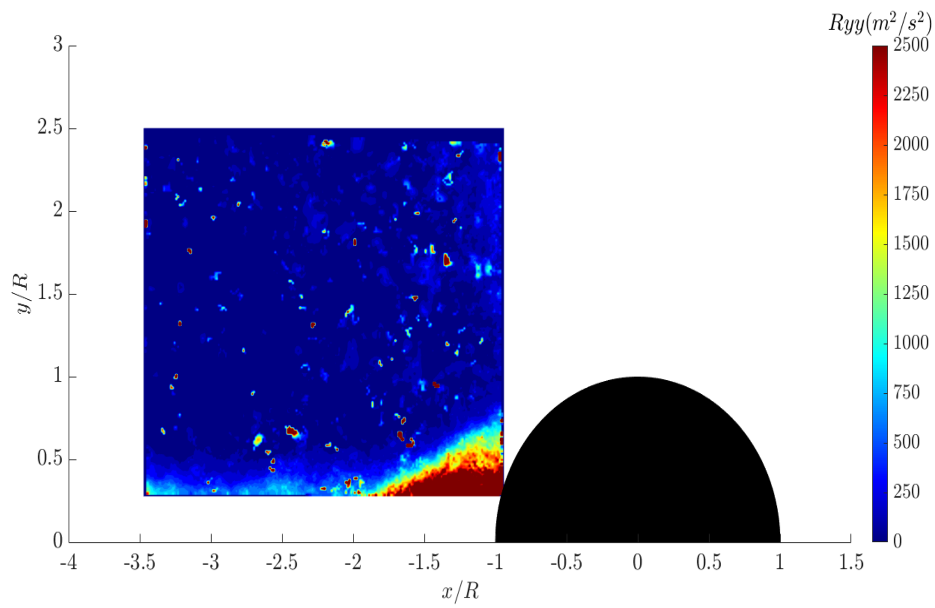

c)

Fig. A4 Reynolds stress Ryy along three spanwise planes: centerline (a), 1.5 mm off center (b), 3.0 mm off center (c)